Experiments and modeling of edge fracture for an AHSS sheet

Citation: Wang, Kai, Meng Luo, and Tomasz Wierzbicki. "Experiments and Modeling of Edge Fracture for an AHSS Sheet." International Journal of Fracture 187, no. 2 (March 11, 2014): 245–268.

As Published: http://dx.doi.org/10.1007/s10704-014-9937-5

Publisher: Springer Netherlands

Persistent URL: http://hdl.handle.net/1721.1/103093

Version: Author's final manuscript: final author's manuscript post peer review, without publisher's formatting or copy editing

Experiments and modeling of edge fracture for an AHSS sheet

Kai Wang*, Meng Luo and Tomasz Wierzbicki

Massachusetts Institute of Technology, Impact and Crashworthiness Laboratory, Department of Mechanical Engineering, Cambridge MA 02139, USA

Abstract

With the emergence of advanced high strength steels (AHSS) and other light-weight materials, edge fracture has been one of the important issues evading reliable prediction using CAE tools. To study edge fracture behavior of AHSS, a comprehensive hole expansion test (HET) program has been carried out on a DP780 sheet. Specimen with three different edge conditions (milled edge, water-jet cut edge and punched edge) are manufactured and tested. Results reveal that the hole-expansion ratio (HER) of the present DP780 sheet is around 38% for milled specimen and water-jet cut specimen, and about 14% for punched specimen. A novel method of a central hole specimen tension is also introduced for edge fracture study, showing a similar trend as found in HET. The paper briefly presents a procedure and the results for a full calibration of the DP780 sheet for plasticity and fracture, where a hybrid testing/simulation method is used to obtain parameters for Hill 48 plasticity model and modified Mohr Coulomb (MMC) fracture model. The finite element simulation gives an accurate prediction of HER, as well as the load displacement response and specimen deflection distribution in the hole expansion tests on uncracked material. The correlation between simulation and tests on central hole specimen also turns out to be very good. The paper also presents a very interesting insight of the initiation and propagation of cracks from the hole edge during a hole expansion test by numerical simulation in comparison with testing observation. The number of final cracks are accurately predicted. Other new aspects of the present paper include an improved 3D DIC measurement technique and a simplified analytical solution, from which a rapid estimation of displacement and hoop strain field can be made (see Appendix B).

Keywords:

Edge fracture, hole expansion test, tension test on specimen with a central hole, MMC model

* Corresponding author, wangkai@mit.edu

This article was intended for the IUTAM Brescia special volume, but could not be processed in time due to editorial and production delays.

1. Introduction

With the immense driving force from cost efficiency and fuel economy, the application of Advanced High Strength Steels and other lightweight materials has been dramatically increased in recent years. An increase of the flow strength has been achieved with a tradeoff decrease in ductility. AHSS usually shows a tendency to fracture at trimmed/blanked edge much earlier than predicted by well accepted Forming Limit Diagram (FLD) (Shi and Chen, 2007). Edge fracture (or called edge cracking, edge splitting) has become a major challenge in stamping of AHSS. It is also becoming an issue in application of aluminum alloys (Stanton et al., 2011).

There has been a lot of published experimental work on edge fracture in the Hole Expansion Test (HET), and this work is briefly reviewed below. The hole expansion test is a popular technique for quantifying the edge stretch limit (Butcher et al., 2013; Chiriac and Chen, 2008; Hyun et al., 2002; Konieczny and Henderson, 2007; Pathak et al., 2013; Shi and Chen, 2007; Shih et al., 2010). The method consists of a pre-machined hole expanded by a punch head until fracture, as illustrated in Fig. 1. During such tests material at the hole edge is subjected to uniaxial tension condition and undergoes hoop stretching all the way until fracture. The hole expansion ratio (HER) reported in such tests gives an easy and straight forward measure of how much the edge has been stretched until fracture. A few testing standards have already been established including: JFS T 1001-96, ISO/TS 16630-2008 (ISO, 2008; JFS, 1996). From hole expansion tests it is observed that generally speaking, punched hole will have a much lower stretch limit compared with machined (milled, drilled or reamed hole) (Konieczny and Henderson, 2007; Pathak et al., 2013; Shih et al., 2010). In view of this, Konieczny (2007) put forward the question on applicability of existing manufacturing method for conventional high strength low alloy (HSLA) steels to new generation of AHSS. A comprehensive experimental study was performed on both HSLA and AHSS steels. Factors including: die clearance during hole punching, bur direction (up or down) during HET test and different machining techniques (milled, laser cut, punched, etc.), were investigated. It turns out that within punched specimen, different die clearances during the punching process yield different HER. Considering the punching process has a great impact on the stretch limit of trimmed edge, Shih et al. (2010) expanded the study to cover factors including new punching techniques by introducing a bevel angle to the punch head, as well as changing sheet material orientation. From these study one important finding that converges is that a die clearance of 15% ~ 20% usually yields the highest HER for AHSS.

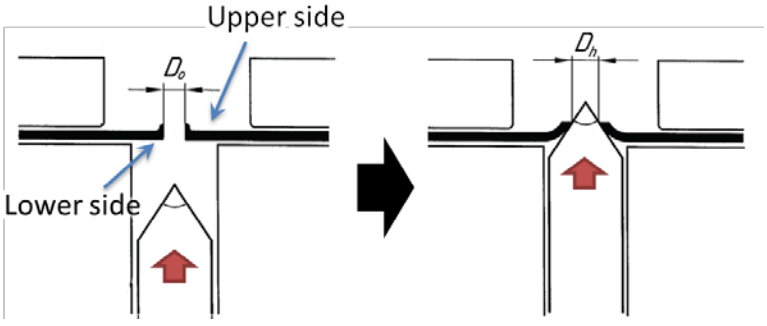

Fig. 1 Schematic of conical hole expansion process (ISO, 2008)

It is believed that the punching process, which shears off part of the material to create the hole, would introduce damage at edge surface and neighboring area, called shear affected zone (SAZ). Butcher et al.(2013) and Chiriac and Shi (2013) tried to quantify SAZ and find

out how much strain hardening has been introduced due to trimming process by micro-hardness test. The results show the total width of SAZ is only about 30% of the specimen thickness. Beyond that the material is kept in a virgin state. This small SAZ gives important clues for edge fracture study. Very interesting methods of calculating the distribution shear strain from the measurement of the flow lines of material during blanking was presented by (Wu et al., 2012).

The recent paper published in the open literature dealing with numerical prediction of HER was due to Butcher et al. (2013) where the original GNT model was used. The effect of shearing/blanking was accounted by the value of initial porosity and strain hardening. The limitation of the GNT model was recently discussed by Dunand and Mohr (2011). All together the calibration procedure presented by Butcher was not clearly explained and the value of parameters appeared to be taken from various papers where different materials were used. The importance of using the same material was emphasized in Section 2 of the present paper.

The recently formulated Modified Mohr–Coulomb (MMC) model by Bai and Wierzbicki (2010) eliminated the limitations of the GNT method and was shown to be applicable in a much wider range of stress triaxiality ($-1/3 \leq \eta \leq 2/3$) for sheets. The model was derived by transforming the stress-based Mohr–Coulomb failure criterion into the space of stress triaxiality, Lode angle and equivalent plastic strain. It has been applied with excellent results to a dual phase steel (Luo and Wierzbicki, 2010), a TRIP steel (Dunand and Mohr, 2011) and to aluminum sheets (Beese et al., 2010; Luo et al., 2012). The MMC model achieves a good balance between complexity/flexibility in capturing the fracture behavior and the simplicity in parameter identification and thus is a natural choice of the present study.

The primary objective of the present paper is to predict initiation and propagation of cracks originated during the hole expansion tests on materials which we considered as uncracked. The amount of pre-damage depends on the technique used to fabricate the holes. Milling or reaming leaves the material around the edge of the hole practically undamaged, while the blanking process produces substantial pre-damage and strain hardening. Tests have been performed on all types of specimen machined by milling, water-jet cutting and blanking, while only milled specimens are the subjects of the present simulation study.

In order to build up a comprehensive database of the material and specimens under investigation, two different categories of tests are performed; one for material characterization and another for edge fracture study. The edge fracture experimental study includes 44 tests of both hole expansion tests and tension tests on central hole specimen. These tests confirmed the trends reported in the literature and provided data for subsequent comparison with numerical simulation. The second category of tests were performed to determine plastic properties of DP780 steel and fracture parameters of the MMC model. All together 22 tests are performed in conjunction with a hybrid numerical and experimental procedure to obtain the material parameters.

The last part of the paper deals with numerical simulation of initiation, propagation and arrest of cracks in hole expansion tests. It is found that due to material anisotropy and random numerical error accumulation, one crack will initiate first and quickly another one will follow and grow. After further loading two more cracks will initiate. Finally a total of four cracks continue to propagate in the radial direction with no more crack initiation. The simulation results are fully consistent with the test observation.

In summary, the paper is reporting on several new important findings regarding the measuring technique and numerical simulation. The authors believe one of the main finding

is the explanation of the mechanism of initiation and propagation of cracks from the free edge. Also an 3D DIC measurement method is introduced in hole expansion tests to obtain the deformation distribution, as well as measuring the HER in comparison with traditional caliper measurement. At the same time, the tension test on central hole specimen is exploited for edge fracture study and compared with the current industry standard of hole expansion test. Finally a simplified analytical solution is presented, from which a rapid estimation of displacement and hoop strain field can be made (see Appendix B).

2. Plasticity testing and modeling

The material under investigation for the present study is a Dual Phase (DP) steel, which serves as a representative grade of advanced high strength steel family. All specimens are extracted from 1.6mm-thick DP780 sheets provided by VoestAlpine (Austria). The exact chemical composition of the present DP780 steel is given in Table 1 as provided by the supplier. Typical microstructure of the DP steels features a soft ferrite matrix and precipitates of martensite as secondary phase.

Table 1: Chemical composition of DP780 used

C	Mn	Cr+Mo	Si	Nb+Ti
0.12-0.16	1.8-2.5	< 0.5	0.5	<0.05

2.1.Anisotropy

A phenomenological approach is adopted in this paper to model plastic deformation and fracture in the framework of uncoupled formulation. Information of plastic deformation given by the plasticity model, together with a calibrated fracture locus, is utilized to calculate damage accumulation and then predict crack formation. Therefore, under monotonic loading, the plastic behavior of the present DP steel sheet is modeled using a standard plasticity theory featuring: (1) an anisotropic Hill'48 (Hill, 1948) yield function, (2) the associated flow rule, and (3) an isotropic hardening law. The yield condition reads

$$f(\boldsymbol{\sigma}, k) = \bar{\sigma}_{\text{Hill}} - k = 0 \tag{1}$$

$$\bar{\sigma}_{Hill} = \sqrt{F(\sigma_y - \sigma_z)^2 + G(\sigma_z - \sigma_x)^2 + H(\sigma_x - \sigma_y)^2 + 2L\tau_{yz}^2 + 2M\tau_{zx}^2 + 2N\tau_{xy}^2}$$

where $\bar{\sigma}_{\text{Hill}}$ denotes the equivalent stress given by the three-dimensional Hill'48 yield function, and k represents the deformation resistance. x, y and z corresponds to rolling, transverse and thickness direction of the sheet material, respectively. The six constants $F \sim N$ are coefficients of anisotropy, and can be identified through proper material tests. The associated/normality flow rule is assumed as

$$d\boldsymbol{\varepsilon}_p = d\bar{\varepsilon}_p \frac{\partial f}{\partial \boldsymbol{\sigma}} \tag{2}$$

where $\boldsymbol{\varepsilon}_p$ is the plastic strain tensor, and the equivalent plastic strain increment $d\bar{\varepsilon}_p$ is defined by the plastic work conjugacy,

$$\boldsymbol{\sigma}: d\boldsymbol{\varepsilon}_p = \overline{\sigma} d\overline{\varepsilon}_p \tag{3}$$

The deformation resistance k is governed by the hardening law

$$dk = H(\overline{\varepsilon}_p) d\overline{\varepsilon}_p \tag{4}$$

The hardening function $H(\overline{\varepsilon}_p)$ is calibrated based on uniaxial tension tests which will be described in details in Section 2.2. Only isotropic hardening is considered in the present study as all of our plasticity and fracture experiments are performed under monotonic loadings.

2.2. Calibration of the plasticity model

The plastic behavior of the present DP780 steel is characterized by means of the uniaxial tensile tests following the ASTM-E8M standard (sheet-type) in three different material orientation α ($\alpha = 0^o, 45^o$ and 90^o), with α denoting the angle between the specimen axis and the rolling direction (Fig. 2). The engineering stress-strain curves of all six uniaxial tensile tests are converted from the load-displacement curves and plotted in Fig. 3a.

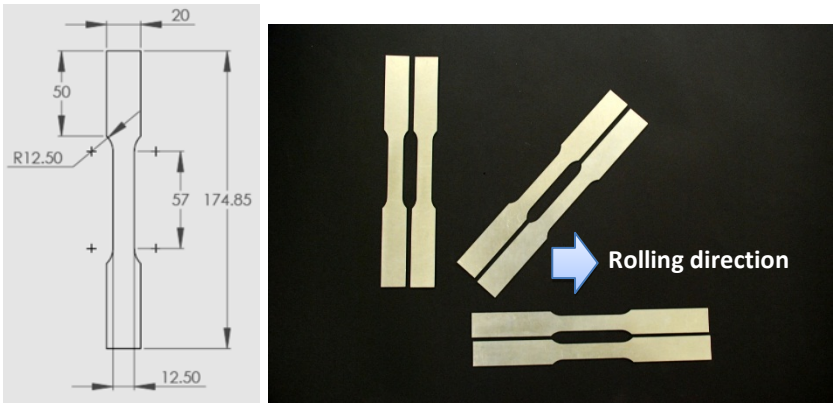

Fig. 2 Geometry of uniaxial tension specimens (dimensions in mm; specimen thickness is 1.6mm). Specimens are cut at $0^o, 45^o$ and 90^o to the rolling direction.

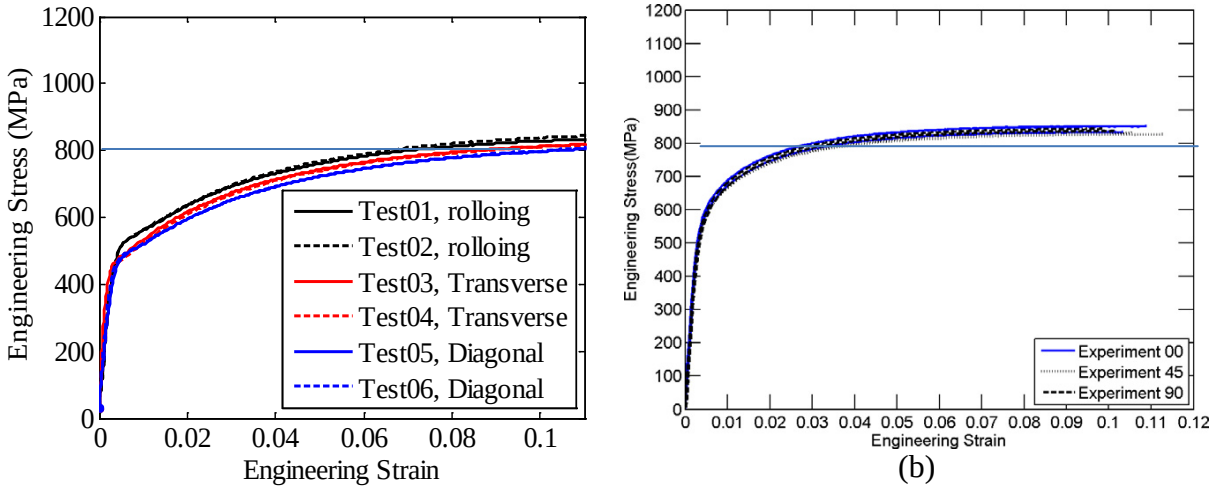

Fig. 3 Stress strain curves of dog-bone tension tests in three directions for DP780 supplied, (a) by VoestAlpine, (b) by US Steel (Luo and Wierzbicki, 2010)

The stress strain curve for the present DP780 steel is compared to seemingly identical DP780 grade provided by US Steel (Luo and Wierzbicki, 2010), see Fig. 3b. While the yield stress for both steels is about the same, there are huge differences in the hardening curve.

To determine the parameters of anisotropy in Eq. (2), the Lankford ratios $r = dE^p_{width}/dE^p_{thickness}$ are then calculated with help from a digital image correlation (DIC) system (VIC-2D, Correlated Solutions, SC). Assuming the associated flow rule, the six Hill'48 model parameters $F \sim N$ are calculated from the Lankford ratios r (Abaqus, 2010) and provided in Table 2. For comparison, the same group of coefficients determined in Luo and Wierzbicki (2010) are also listed in Table 2.

Table 2: Hill'48 coefficients determined from average *r*-value of DP780

Supplier	F	G	H	L	M	N
VoestAlpine	0.6619	0.5872	0.4128	1.5	1.5	1.8029
US Steel	0.56	0.56	0.44	1.5	1.5	1.5

It should be noted that each new material need to be individually calibrated even if they are listed as the same grade. There are no text book properties for a DP780 grade and the above remark is true for many other grades of aluminum and steels. The above comparison justifies why so much attention was given in the paper to characterization of this particular material rather than taking data from the literature.

Isotropic hardening rule as described by Eq. (5), is also a key ingredient of the plasticity model. The true stress-strain curve up to the necking point (true strain 0.17) for a uniaxial tensile specimen along rolling direction is depicted in Fig. 4a with black open dots. It is shown that the Swift law (power law)

$$k = A(\varepsilon_0 + \bar{\varepsilon}_p)^n \tag{5}$$

provides a good approximation for the true stress strain curve during the stage of uniform elongation, as demonstrated by the blue broken curve in Fig. 4a. The corresponding Swift law parameters are given in Table 3.

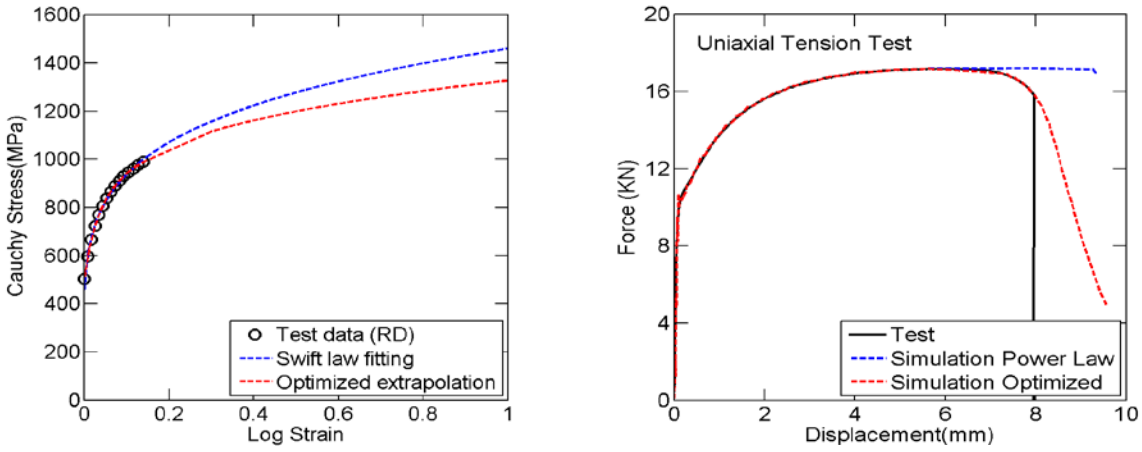

(a) (b)

Fig. 4 Identification of a reliable strain hardening curve to large strains. (a) Choices of the strain hardening extrapolations. (b) Predictions of the force-displacement response using different stress-strain curves. Refer to Table 3 for the Swift law parameters.

However, the Swift law extrapolation is verified only up to the necking strain. Thereby, an inverse approach reported by Dunand and Mohr (2010) and Luo et al. (2012) is taken to extend the hardening curve to larger strains based on the uniaxial tensile data in rolling direction. The resulting optimized extrapolation of stress-strain curve accurately captures the post-necking portion of the load displacement response in simulation (red broken curve in Fig. 4b) and will be used in all simulations in the following sections.

Table 3: Swift hardening law parameters for the DP780 steel

A [MPa]	ε_0[-]	n [-]
1460.3	0.0024	0.1943

3. Fracture characterization for un-cracked material

In this study, an uncoupled phenomenological approach is employed to model the ductile fracture of the un-cracked DP780 sheets. The damage accumulation and crack formation are modeled independently of plasticity equations using a Modified Mohr-Coulomb (MMC) fracture criterion (2010). A comprehensive experimental program is carried out to characterize the fracture behavior under multi-axial loadings and an inverse approach is adopted to calibrate the parameters of the fracture model considering the entire loading history.

3.1.Fracture modeling

Following several successful applications (Beese et al., 2010; Dunand and Mohr, 2011; Luo et al., 2012; Luo and Wierzbicki, 2010), the damage accumulation is defined by the following scalar function

$$D(\bar{\varepsilon}_p, \eta, \bar{\theta}) = \int_0^{\bar{\varepsilon}_p} \frac{d\bar{\varepsilon}_p}{\hat{\varepsilon}_f(\eta,\ \overline{\theta})} \tag{6}$$

where the integral of the weighted equivalent plastic strain is regarded as a damage indicator D. The weighting function $\hat{\varepsilon}_f$ is usually termed as the 'fracture envelope', which defines the fracture strains of the un-cracked material under all possible monotonic proportional loadings. Equation (7) implies that a given increment of the equivalent plastic strain $d\overline{\varepsilon}_p$ contributes to the damage accumulation in a linear incremental way depending on the current stress state, which is fully characterized by stress triaxiality η and Lode angle parameter $\bar{\theta}$. It is assumed that the at the point of fracture initiation, $\bar{\varepsilon}_p = \bar{\varepsilon}_p^f$ and $\mathrm{D} = 1$. Within this phenomenological framework, the function $\hat{\varepsilon}_f(\eta,\ \overline{\theta})$ is highly non-linear and is either chosen empirically or its form follows from micromechanical consideration.

Bai and Wierzbicki (2010) derived a novel fracture envelope by transforming the classical stress-based Mohr-Coulomb failure criterion, into the space of stress triaxiality η, Lode angle parameter $\overline{\theta}$ and equivalent plastic strain $\overline{\varepsilon}_p$. The functional form of MMC fracture envelope reads

$$\hat{\varepsilon}_f = \left\{\frac{A}{c_2}\left[c_3 + \frac{\sqrt{3}}{2-\sqrt{3}}(1-c_3)\left(\sec\left(\frac{\overline{\theta}\pi}{6}\right)-1\right)\right]\left[\sqrt{\frac{1+c_1^2}{3}}\cos\left(\frac{\overline{\theta}\pi}{6}\right) + c_1\left(\eta + \frac{1}{3}\sin\left(\frac{\bar{\theta}\pi}{6}\right)\right)\right]\right\}^{-\frac{1}{n}} \tag{7}$$

The constants c_1, c_2 and c_3 are three free parameters which should be calibrated through fracture tests. As shown in Fig. 9, the geometric representation of the MMC fracture envelope is half-tube which is asymmetric with respect to $\overline{\theta} = 0$, and monotonically decreasing with η.

3.2.Fracture testing

An extensive fracture testing program featuring four different types of tests, i.e., tension tests on notched specimens, tension tests specimens with central hole, equi-biaxial punch tests and biaxial tests on butterfly specimen, are carried out (Table 4). The introduction of various tests is to cover a vast range of stress states.

Except for the equi-biaxial punch test, which is performed on a 200kN MTS universal servo-mechanical loading frame, all other tests are carried out on a custom-made dual actuator loading frame (Instron Model 8080) as schematically shown in Fig. 5. The machine is capable of applying both vertical and horizontal load under displacement control or force control. Specimen featured wide shoulders are fixed in specially designed clamping device to guarantee good alignment and high clamping pressure. Digital Image Correlation (DIC) is used throughout all tests to record displacement field on specimen. After each test, the corresponding load displacement response up to the point of fracture is obtained as illustrated in Fig. 6. More results are summarized in Fig. A1 in Appendix A.

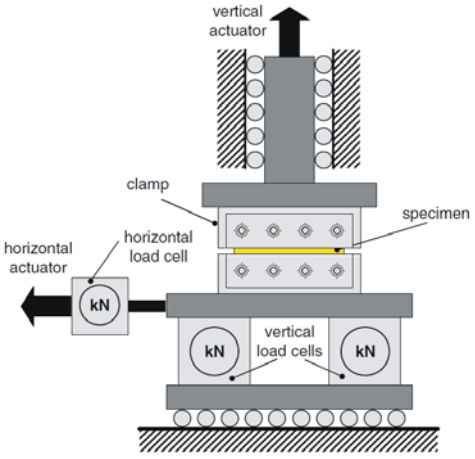

Fig. 5 Schematic of dual-actuator loading frame(Mohr and Oswald 2008)

Table 4 Summary of tests for fracture calibration

NO.	***Test***	***Initial η***
	Notched specimen tension	
1	*R6.67*	0.3835
2	*R10*	0.3667
3	*R20*	0.35
4	Tension on specimen with a central hole	0.33
5	Equi-biaxial test (spherical punching)	0.66
	Butterfly specimen test	
6	*Pure shear*	0
7	*Combined tension and shear*	0.2
8	*Plane strain*	0.5

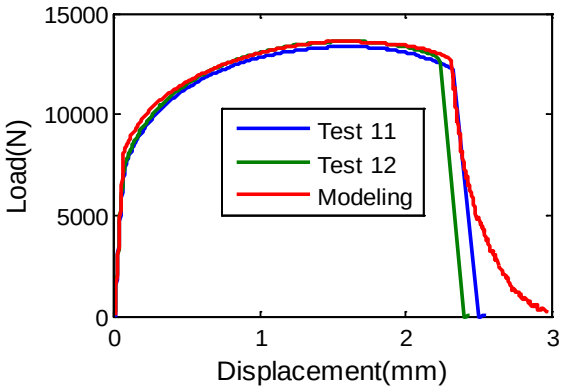

Fig. 6 Load displacement response of tension tests on notched specimen with cutout radius of R=20mm

The readers are referred to Dunand and Mohr (2010) for detailed discussion on tension test of notched specimen as well as tension on specimen with a hole in the center, to Beese et al. (2010) for equi-biaxial test and Beese et al. (2010), Luo and Wierzbicki (2010) for tests on butterfly specimen.

3.3.Fracture model calibration

A hybrid experimental and numerical procedure is then carried out to obtain information needed for fracture model calibration including evolution of plastic strain ($\bar{\varepsilon}_p$), the corresponding stress triaxiality η and lode angle parameter $\bar{\theta}$, as described in Dunand and Mohr (2010). To do this, explicit finite element simulations were performed for each fracture test detailed in Section 3.2 using Abaqus/Explicit. Force-displacement curves are extracted from each simulation and compared with the experimental measurements (Fig. 6). As illustrated in Fig. 7, the gauge points in the FE models (the red dots denoted by 'Displ out') are consistent with the positions of virtual extensometers used in the DIC during post-processing experimental data. The critical element corresponds to material points where fracture initiation is observed during the tests.

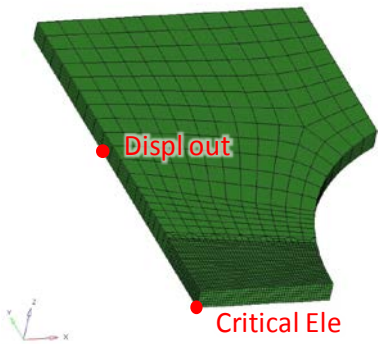

(a)

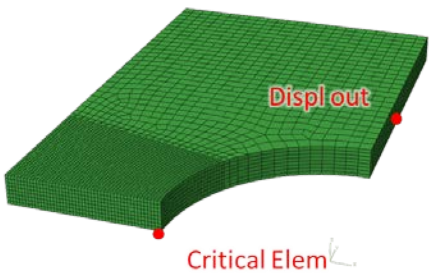

(b)

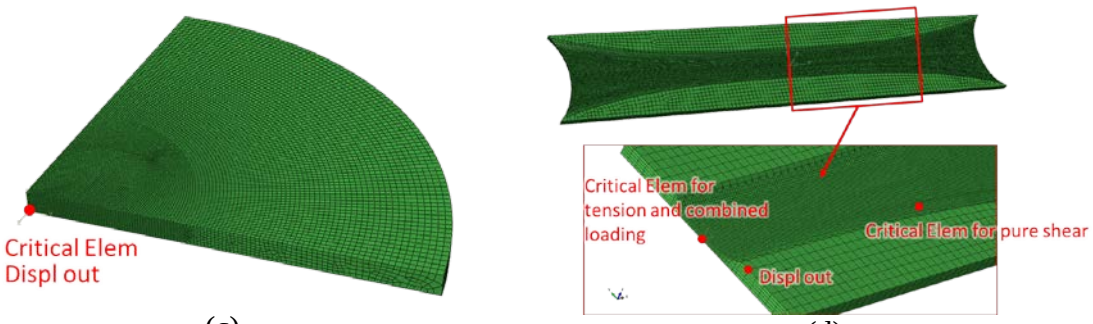

(c) (d)

Fig. 7 FE mesh for each of the four fracture specimen and locations of critical elements for fracture initiation: (a) notched tension specimen, (b) tension specimen with a center hole, (c) equi-biaxial punch disk specimen (d) biaxial butterfly specimen.

Fig. 8 shows the evolution of the equivalent plastic strain ($\bar{\varepsilon}_p$) as a function of η and $\bar{\theta}$ at the critical material points from all eight fracture experiments. All the fracture points in Fig. 8 correspond to the experimentally determined fracture initiation points. These loading paths are also plotted in the space of ($\bar{\varepsilon}_p$, η) in Fig. 8b. It is seen that the present fracture testing program covers a large range of stress states in terms of both η and $\bar{\theta}$.

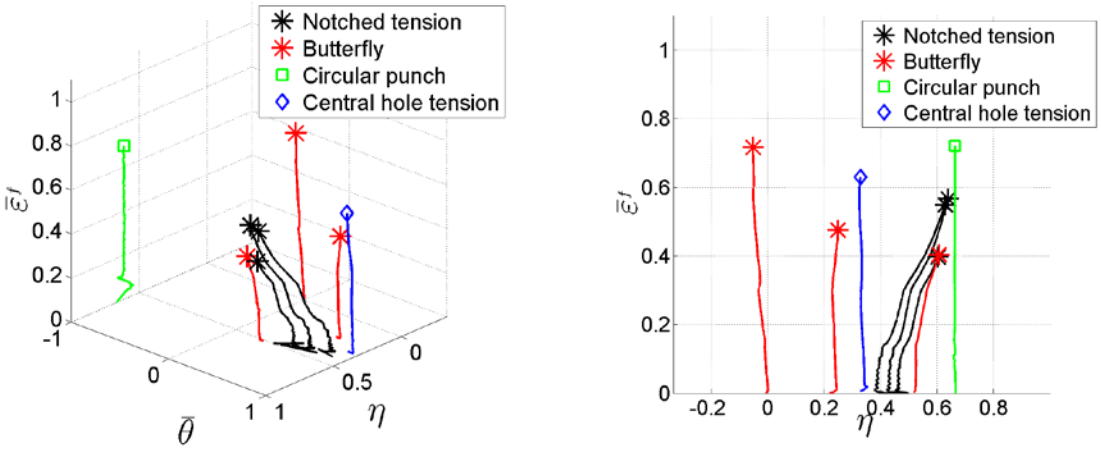

(a) (b)

Fig. 8 Loading paths at the critical material points of the specimens: (a) for all eight experiments in the space of ($\bar{\varepsilon}_p$, η, $\bar{\theta}$); (b) for all eight experiments in the space of ($\bar{\varepsilon}_p$, η).

The fracture parameters c_1, c_2 and c_3 in Eq.8 are then obtained from the data plotted in Fig. 8 using a least square error (difference between damage D calculated from Eq.7 and unity) optimization procedure developed by Luo et al. (2012). The parameters are listed in Table 5. The corresponding MMC fracture envelop is plotted in Fig. 9.

Table 5. Parameters of the calibrated MMC fracture model for DP780

c_1 [-]	c_2 [MPa]	c_3 [-]	Least Square Error[-]
0.107	757.8	0.972	0.0134

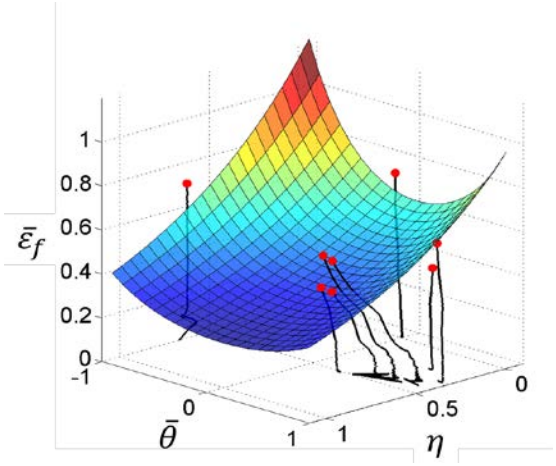

Fig. 9 MMC fracture envelope for the present DP780 steel showing the equivalent strain to fracture as a function of the stress triaxiality and the Lode angle parameter. The black trajectories denote the loading path of the eight experiments which are used for calibration.

Simulation results for all fracture calibration tests are plotted in Fig. 6. They all show a good correlation with the corresponding test results, proving our plasticity model and fracture model to be valid to use. It should be noted that due the statistical nature of multiple fracture initiation points around the hole edge in hole expansion tests calls for the lowering fracture locus around $\eta = 1/3$ corresponding to uniaxial tension, which is done by taking hole expansion test as a calibration test and used in simulation.

4. Edge fracture experimental study

The following sections will carry out tests specifically designed for edge fracture study including hole expansion tests and tension test on specimen with a central hole, followed by results from the corresponding numerical simulation on uncracked material.

4.1. Hole expansion test

As shown in Fig. 1, when the punch head moves through a disk with a hole in the center, the hole edge is stretched until fracture. The hole expansion ratio (HER) as defined by Eq.9 is nothing but an average engineering measure of hoop strain after fracture, providing a simple and convenient way to rank the various materials in terms of edge stretchability.

$$HER = \frac{D_h - D_0}{D_0} \tag{8}$$

where D_h is the inner hole diameter after test and D_0 is the original hole diameter before test.

Three types of manufacturing techniques were used in the present study to fabricate hole edge which are milling, water jet cutting and punching/blanking. Milled edge is believed to keep the actual properties of material the best. This method is carefully applied to introduce as little pre-damage to the hole edge as possible. At the same time, with good cooling condition there is no heat affected during machining. Water jet cut is an abrasive cutting technique and yields a rough surface. Punching (or called blanking or trimming) is very popular in industry for mass production because of its high efficiency, low cost and relatively good quality. However, edges fabricated this way are left with a severe pre-damage and residual strain, thus are prone to edge fracture in the following forming process.

The tool setup for hole punching/blanking process is illustrated in Fig. 10. An important parameter during this process is die clearance "CL", which is the gap between punch head and die normalized by thickness of specimen as defined in Eq. 10. In the current study, three different CL's which are 5%, 10% and 20%, are used. There are five repeats for milled specimen and water jet cut specimen, while four repeats for each die clearance of punched specimen.

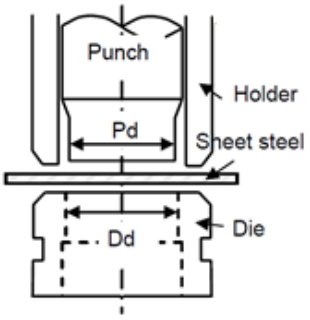

Fig. 10 Schematic of punching tools (Shih et al., 2010)

$$CL = \frac{D_d - P_d}{2t} \tag{9}$$

4.2. Test procedure

Punch head

Different shapes of punch head have been reported in literature including conical punch, flat punch and spherical punch. They introduce different loading conditions that result in different strain gradients in specimen during testing. Conical punch head is recommended by ISO 16630 in which case the hole edge will undergo maximum stretch during the test. The specimen goes through a large rotation when the edge is stretched, yielding non-uniform strain at different locations through thickness and radius. Flat punch produces a loading condition that is very close to stamping process in manufacturing. There is no rotation on the specimen close to edge, but the stress state in the material favors a fracture to happen away from the edge, rendering the fracture limit depends more on the material properties instead on edge stretch limit. Spherical punch head yields a loading condition on specimen between that produced by flat punch and conical punch in sense of specimen rotation and fracture location.

In the current study, geometry of the punch head as well as of the fixtures is chosen in accordance with ISO 16630. Punch head has an angle of 60 degrees with the column diameter of 28mm. The die diameter is 50mm with a round edge radius of 1mm. Fig. 11 shows the test setup and the clamping tool.

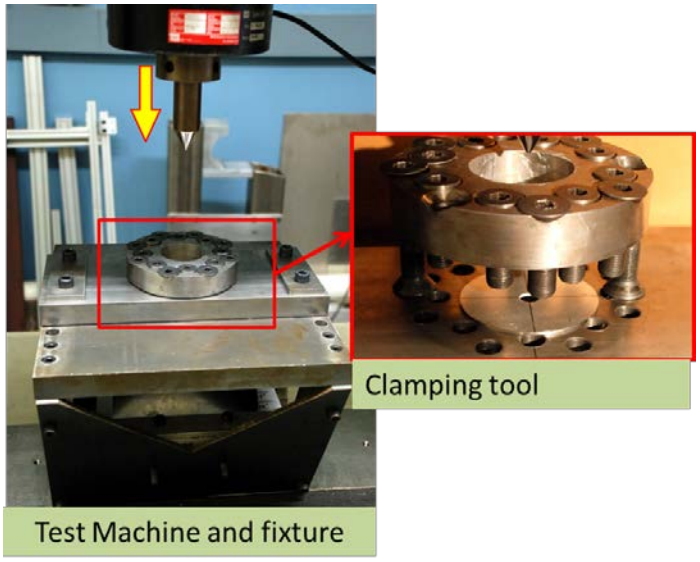

Fig. 11 Test machine set up and clamping tool for hole expansion test

Clamping: As illustrated by Fig. 11, the disk specimen is clamped on the lower die by a 25mm thick metal ring through sixteen M10-12.9 bolts. Each bolt is tightened to a torque of 65NM before test. This clamping force makes sure that no slipping is observed during the test.

Alignment: The specimen is placed in a bur-up position for punched specimen, meaning the bur stays away from the punch head instead of in contact with it. Before tightening the clamping ring, the conical punch head is moved in contact with the specimen with an axial force of 100N to make sure the coaxiality between specimen and the punch head.

Procedure: Tests are carried out on a universal testing machine (MTS G45) at displacement control mode, with crosshead velocity of 2mm/min. The test is stopped while first through thickness crack happens. HER is then reported by measuring hole diameter of the specimen. Since the specimen rotates during the test, the specimen surface in contact with the punch head (we call it lower side from now on for convenience, Fig. 1) is under less elongation compared with the surface away from punch head (called upper side). The inner hole diameter measured from lower side is used for HER calculation.

Issue of overshoot: During the test, operator usually observes the edge with bare eye and stop the test manually when the first through thickness crack is observed. However, since cracks are very tiny and not easy to observe, hole expansion tests are usually stopped when the crack is already quite obvious, resulting in over-shooting of punch head and larger HER. Also, crack can happen anywhere at the hole edge because of geometrical and loading symmetry, making it even more difficult to find the first through thickness crack. As a result, there is a usually a considerable discrepancy in HER reported by different researchers. Even the result reported by the same operator has a large variation from test to test (Chiriac and Chen, 2008; Konieczny and Henderson, 2007; Shih et al., 2010).

To overcome the problem of overshooting and to reduce variation in test results, A 3D DIC non-contact measuring method is introduced. Two cameras were used to monitor the specimen and record images throughout the test. Due to the limited space below the fixture, a mirror with silver layer on top of the glass is introduced to reflect the specimen into camera

(Fig. 12). The 3D DIC will improve the test result in two aspects. Firstly, with the assistance from cameras, the hole edge is magnified by more than 10 times on the monitor, making it much easier to determine when first through thickness crack occurs. Secondly, 3D DIC is capable to obtain the deformation on the surface of the specimen despite the deformation happens in a 3D space due to the large rotation and out-of-plane displacement. This gives the capability of checking images frame by frame to specify the exact time when first through thickness crack happens and calculating HER at that time.

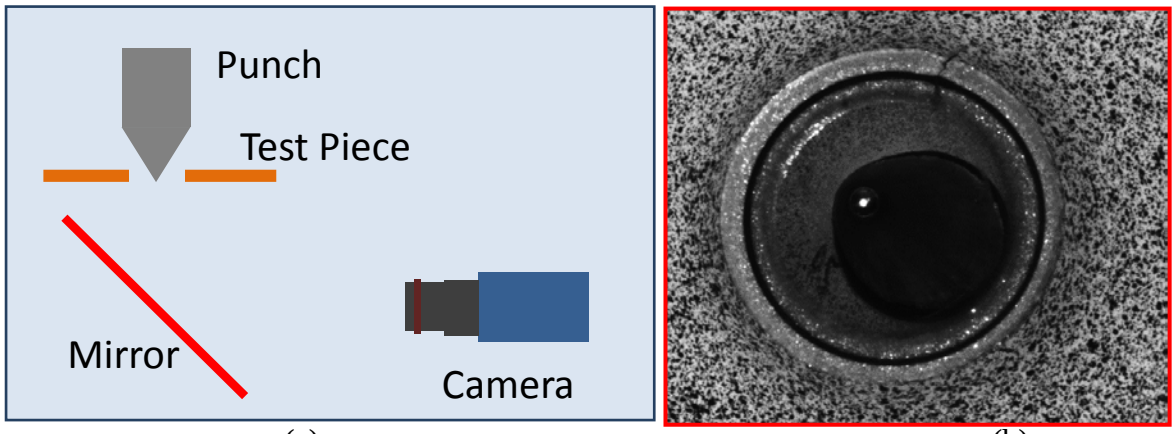

(a) (b)

Fig. 12 (a) Schematic of camera arrangement in a hole expansion test, (b) captured image of specimen after fracture observed

4.3. Test results

With help from cameras to observe the hole edge in real time, the tests are able to be stopped in time after the first through thickness crack develops. Therefore HER values are obtained by measuring hole diameter using caliper with smaller variation. The results are summarized in Table 6. It shows that milled specimen and water jet cut specimen can be stretched by almost 40% before fracture, while punched specimen can only be stretched by about 15%. Milled specimen has a stretch limit of 37.5%, a little higher than 35% of water jet cut specimen. For punched specimen, different die clearance yields different edge stretch limit and 20% die clearance in this case gives the highest HER. But the difference between different die clearances is very small, and is close to the standard variation of test results.

Table 6 Summary of HER from hole expansion tests

	Punched specimen			**Milled**	**Water jet cut**
	CL=20%	CL=10%	CL=5%		
HER	0.161	0.139	0.121	0.378	0.349
Standard Deviation	0.018	0.013	0.014	0.019	0.015

The above results are fully consistent with the findings of many authors in past (Chiriac and Chen, 2008; Konieczny and Henderson, 2007; Pathak et al., 2013; Shi and Chen, 2007; Shih et al., 2010).

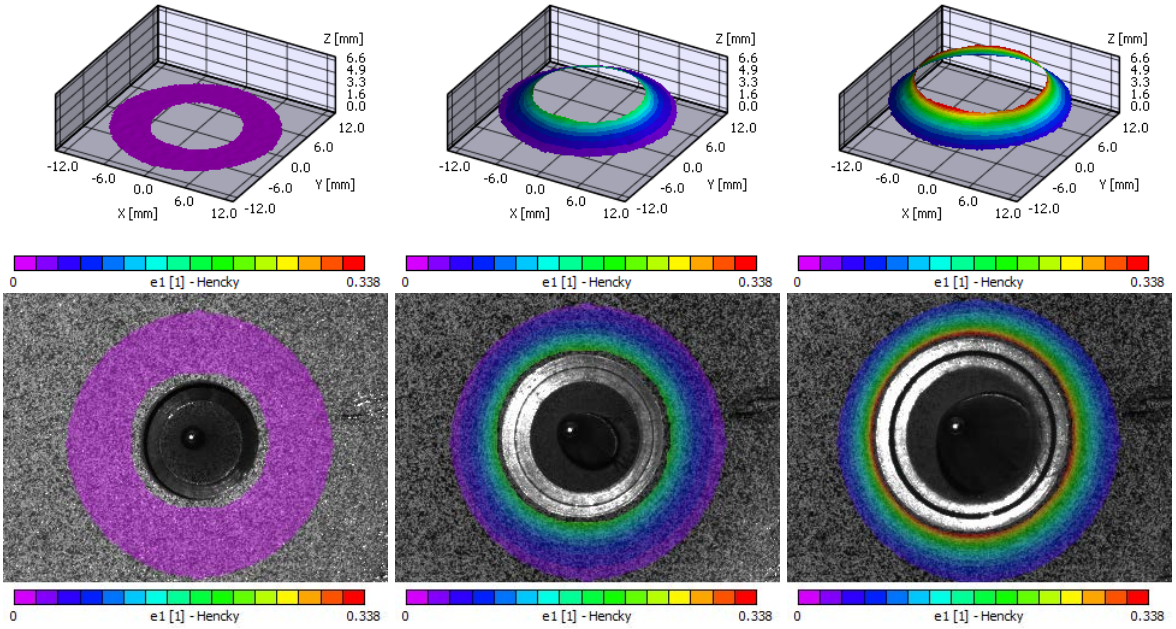

(a) (b) (c)

Fig. 13 Contour plots of major logarithmic strain at three different punch head displacements during a hole expansion test measured by 3D DIC, isometric and top view

Figure 13 shows the contour of the hoop logarithmic strain calculated by 3D DIC during a hole expansion test. It is observed that the maximum stretching always locates at the hole edge. Also there is no obvious strain localization around hole edge hoop direction before fracture.

The 3D DIC system is also capable of measuring HER. However, it consumes substantial time to do this while the main improvement compared with a caliper measurement, which is less variation in the measured HER, turns out to be not so substantial. More discussions is provided in Section 6.1.

4.4. Tension test on central hole specimen

The tension test on central hole specimen is still a new tool for edge fracture study. The specimen features a parallel gauge length with width of 20mm and a hole with diameter of 10mm in the center (Fig. 14a). When subject to tension, the deformation concentrates at the hole edge in the middle cross section and crack is observed to initiated from there in all tests (marked by the red square in Fig. 14a). Numerical analysis shows the stress triaxiality in material at hole edge stays almost constantly at 0.33 throughout the test at the edge (Dunand and Mohr, 2010; and Luo, 2012), meaning the stress state in critical material elements is the same as that in hole expansion test. The same testing program as hole expansion tests is carried out, which includes five milled specimen, five water jet cut specimen and twelve punched specimen with three different die clearances (four specimen four each die clearances, including 5%, 10% and 20%).

A 2D DIC is used to measure the deformation on the specimen surface. To do this a random speckle pattern is prepared beforehand with speckle size of order of 100um. Two cameras are used with one camera capturing the whole specimen gauge length while the other one concentrating in the local area of the hole to obtain a better resolution. The specimen was

subjected to the biaxial loading frame (Fig. 5) and loaded under a constant piston speed of 0.4mm/min until a crack is observed at the hole edge.

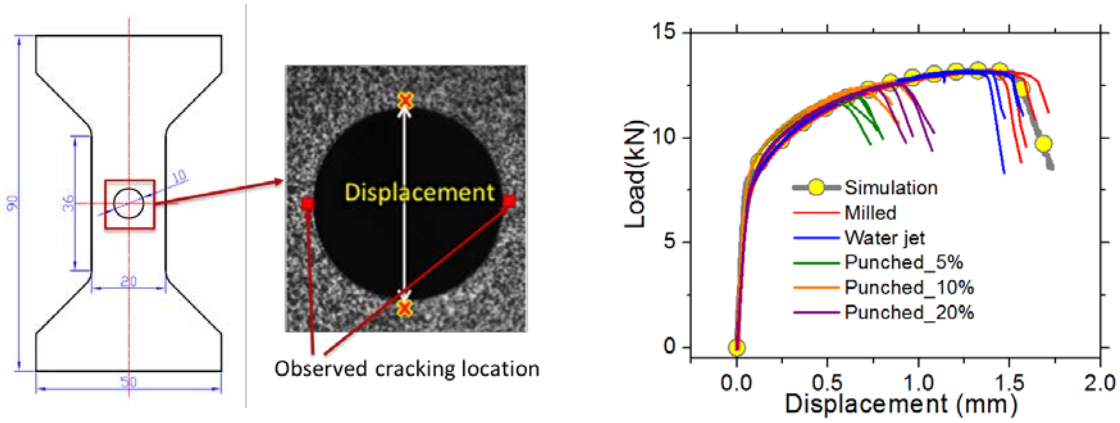

(a) (b)

Fig. 14 (a) Specimen schematic diagram of the central hole specimen, and the locations to extract displacement results in DIC. (b) Load displacement response from the tensile test.

Load displacement curves from this group of tests are shown in Fig. 14b. The displacement data is measured by 2D DIC from the highest and lowest points in tensile direction on the hole edge (Fig. 13a). The logarithm axial strain contours are also obtained and plotted in Fig. 15. It is observed that:

1. Deformation above and below the hole is relatively small at about 0, while the deformation mainly concentrates in the two branched left and right to the hole.
2. At the same time within the two branches, strain concentrates on the hole, indicating that it is the critical area in such a test.
3. Cracks are observed to initiated at the hole edge when fracture happens.

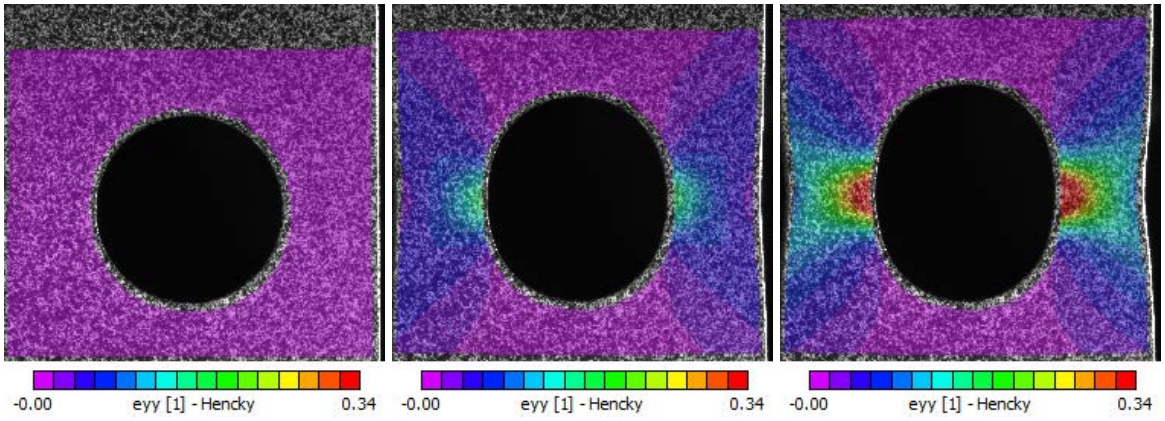

(a) (b) (c)

Fig. 15 Contour plots of logarithmic axial strain (tensile direction) at three different piston displacements during a tension test on central hole specimen

It's found from tests that the observable crack happens at the edge when load curve drops in Fig. 14b, which enables us to use the load displacement curve turning point as the indicator of fracture. Taking the displacement at fracture as a measure of fracture limit, it is obvious that milled specimens have the largest edge stretch limit (red curves in Fig. 14b) and specimens with punched hole have a much smaller one (orange, green and purple curves in Fig. 14b). Fracture limit of water jet cut specimens (blue curves in Fig. 14b) are a little smaller than milled specimens. For punched specimen, 20% die clearance results in the highest stretch

limit while 5% die clearance yields the lowest one. It is exactly the same trend as observed in hole expansion tests.

5. Finite element modeling

5.1. Model description

Numerical analysis is performed on both hole expansion tests and tension tests on specimen with central hole. The simulations were carried out assuming the virgin state of material, which corresponds to the testing on carefully milled specimen. The anisotropic plasticity model outlined and calibrated in Section 2, together with the MMC fracture model described and calibrated in Section 3 are implemented as a user material subroutine in Abaqus (VUMAT) in all following simulations in the present study. Explicit finite element simulation is carried out with the loading velocity and material density chosen such that at least 500,000 time steps are completed. Furthermore, during all simulations, the kinetic energy of the models has been checked to ascertain that it does not exceed 1% of the total internal energy of the model, and thus no dynamic effects have been introduced while using explicit solver.

To fully exploit the geometric and loading symmetry and material orthotropy, only a quarter of the hole expansion specimen (Fig. 16) and one eighth of the specimen with a central hole (Fig. 7b) are modeled. The specimen is discretized using reduced-integration eight-node solid elements (type C3D8R from the Abaqus element library). The mesh is made such that the elements at the critical region close to hole edge where maximum stretching or localization happens have an aspect ratio of 1:1:1 and an edge length of about 0.1mm.

In simulation on hole expansion test, considering the good clamping condition of the specimen and intermediate load level (peak load of measured is about 15kN), a fully clamped boundary condition is assigned to the specimen perimeter. A symmetry boundary condition is imposed on both sides which corresponds to planes of symmetry. The conical punch head is modeled as analytical rigid body and confined to move only in axial direction to expand the hole. Contact between punch head and specimen is assumed to be frictionless.

In simulation on tension of central hole specimen, due to the ideal rigidity and alignment of the load frame as well as of the clamping tools, a symmetry boundary condition is applied on each of the three symmetry planes. A displacement boundary condition is applied on the upper side plane to give the specimen a tensile loading.

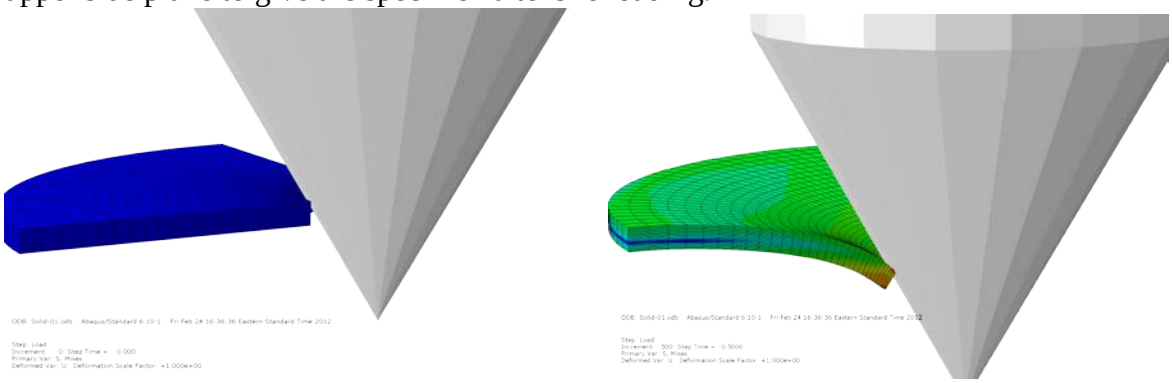

(a) Undeformed model (b) Deformed model

Fig. 16 Finite Element model used for hole expansion test simulation

5.2. Simulation results

Punch head displacement and reaction force data are extracted after simulation and compared with testing results in Fig. 17 for hole expansion tests. At the same time the out-of-plane deflection of each material point is obtained by 3D DIC and the distribution with respect to different distance to the hole center is plotted in Fig. 17b in comparison with the simulation results. The simulation gives a prediction with good accuracy for both load displacement response and the deflection distribution, further proving the validity of the plasticity model.

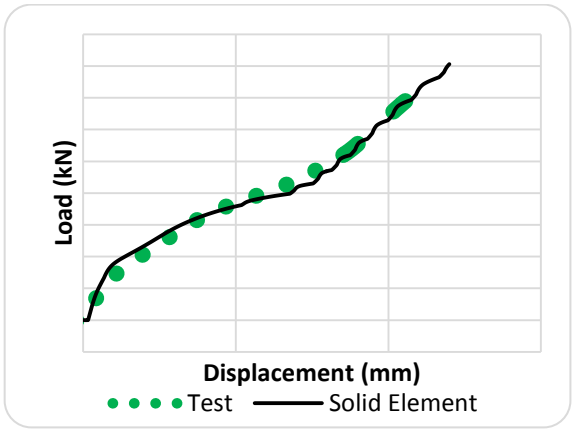

(a)

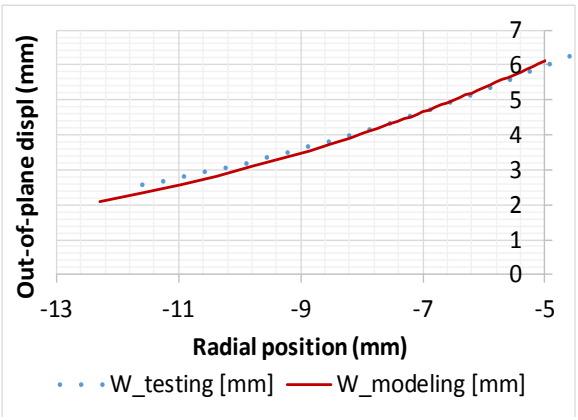

(b)

Fig. 17 (a) Load displacement response of hole expansion test, testing vs. simulation (black solid curve), (b) distribution of out-of-plane deflection with respect to distance to hole center at fracture

In simulation of tension tests on central hole specimen, the load displacement response is compared with test results in Fig. 14b. To check the accuracy of prediction on deformation localization, a local extensometer of initial gauge length of 0.2 mm is taken 0.2 mm away from the hole edge (Fig. 18a) is introduced. The engineering strain measured by this local extensometer is extracted from both the testing results using 2D DIC and from FE simulation. The results are compared in Fig. 18b, where the horizontal axis is overall displacement illustrated in Fig. 14a. In addition, the logarithmic strain in the middle cross section (Fig. 18a) on the surface of the specimen is also obtained from both simulation and testing and compared in Fig. 18c. These results clearly shows that the numerical simulation gives a good prediction for both the overall load displacement response and the localized deformation.

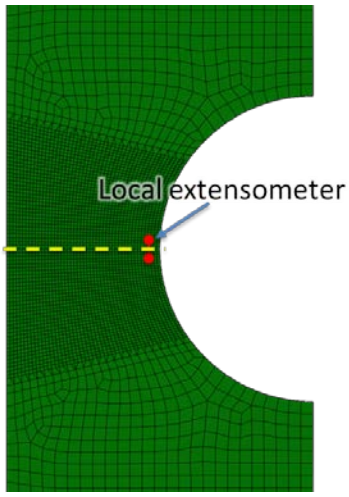

(a)

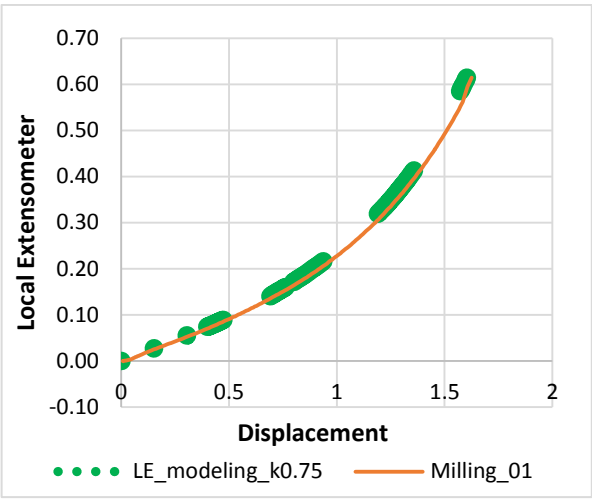

(b)

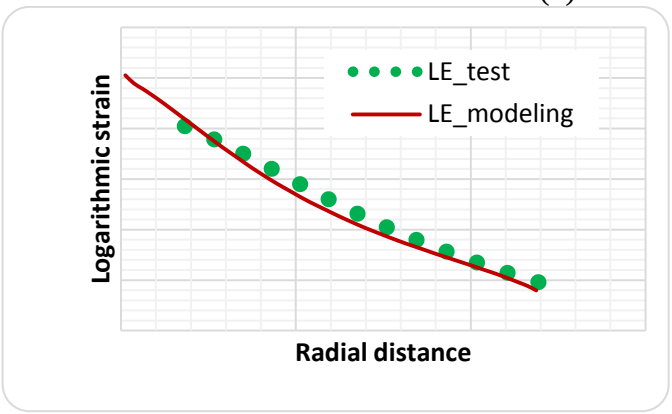

(c)

Fig. 18 (a) Local extensometer marked by the two red dots, and the middle cross section marked by a yellow dashed line, (b) Local deformation history with respect to the overall displacement, (c) Strain distribution in the middle cross section (yellow dashed line in (a)) right before crack is observed. Radial distance is measured from the hole edge

6. Results and discussions

6.1. Application of non-contact measurement in HET

Due to difficulties in detection of first through-thickness crack, the measured HER usually includes error from overshoot of punch head. However a non-contact measurement system, like VIC-3D (Correlated Solutions, SC) can help to minimize this error. During the test a series of images were taken of the hole edge. After test, the images are checked frame by frame to measure the diameter change using VIC-3D from the first frame that the through thickness crack is detected.

To determine the hole diameter, VIC-3D measures distance between two points on the specimen (Fig. 19a). Due to the innate constraint of VIC-3D, points right at the edge of the hole cannot be calculated because VIC-3D requires a point to have speckle patterns in the vicinity all around it. One can only track points away from the edge with a distance of half the subset size, which is 31 pixels in current study. At the same time the point is on the surface away from conical punch head, while measuring HER requires measuring inner diameter from surface in contact with punch head. To correct this measurement, the ratio of displacement at point 1 over that of point 2 is obtained from finite element simulation and plotted in Fig. 19b. Point 1 is the point right at the edge on the surface in contact with punch head corresponding to the point where the HER should be measured. The displacement at this point measures the increment of hole inner radius, denoted as d1 in Fig. 19c. Point 2 corresponds to the point that can be measured in VIC-3D and displacement extracted here is denoted as d2 in Fig. 19c. Then the result measured in VIC-3D corresponding to point 2 is scaled by the ratio found in FEA to get the hole diameter increase and calculate HER.

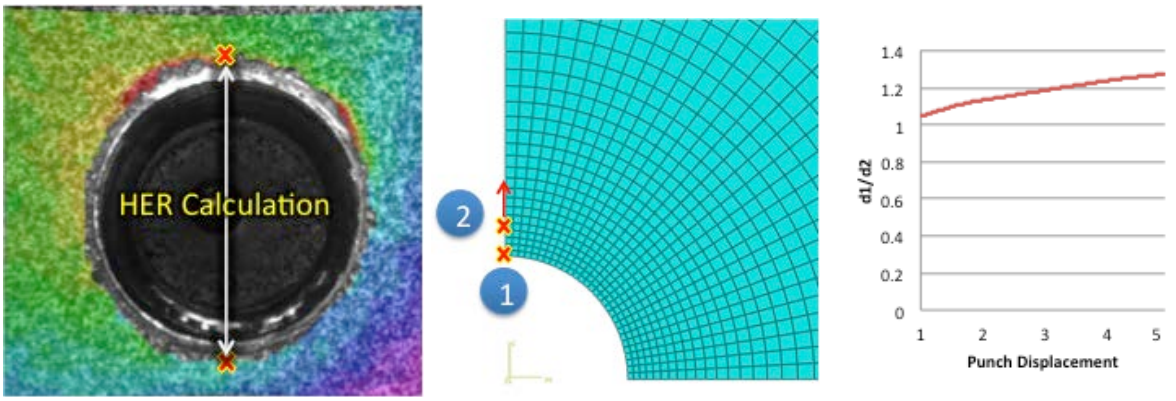

(a) (b) (c)

Fig. 19 Correction of the inner hole diameter measured from DIC. (a) points measured in DIC, (b) points tracked in FE analysis, point 1 is at hole edge, point 2 correspond the pixel tracked in DIC, (c) ratio of diameter measured at point 1 and point 2 as a function of punch displacement

HER results from mesurement of hole diameter using a caliper after test and from 3D DIC on the last frame before fracture are compared in Fig. 20. 3D DIC measured results have slightly smaller normalized standard variation (defined as the standard variation normalized by the average value) of 4.7%, compared with that of 6.0% for caliper measured results. The mean value measured by 3D DIC is a bit smaller because there is still a little overshoot in the test included by the caliper measured results.

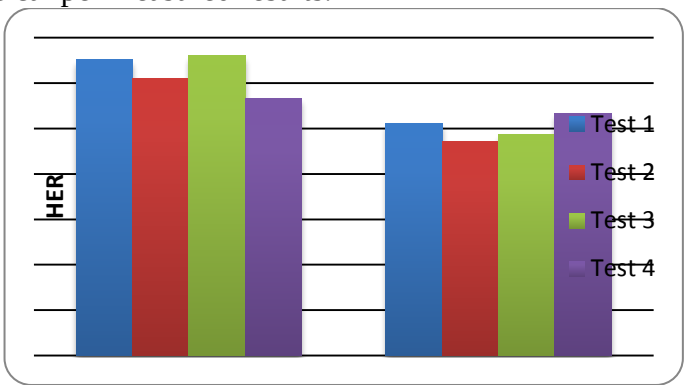

Fig. 20 HER in four tests on water jet cut specimen

Despite the fact that 3D DIC eliminates overshoot from the measured HER and reduced the variation, the improvement is relatively insignificant. With the help of a camera to magnify the hole edge and observe it in real time, the overshoot as well as variation in test results are already greatly reduced. At the same time, using 3D DIC to measure HER is a very time consuming process, which is due to the time consuming system calibration and setup procedures and data processing efforts. Therefore during hole expansion test, the HER is measured by 3D DIC in only two tests out of the total of 44. For the majority of hole expansion tests, a much simpler HER measurement using caliper, with a camera to help observe the hole edge in real time during the test, is recommended. However 3D DIC is still useful in providing a detailed deflection and deformation field (Fig. 17b), which cannot be obtained by the caliper or a 2D DIC (one camera) method.

6.2. Interpretation of test results from central hole specimen tension tests

In the hole expansion test the specimen hole undergoes almost uniform stretching. A careful inspection on the specimen after test reveals that there is no obvious localized necking around

the crack at hole edge, as shown in Fig. 21. Therefore, hole expansion ratio HER makes a natural measure of the stretch limit of the material. It is simply an engineering measure of final hoop strain of the hole after crack initiates. It needs to be point out that the HER value is measured from the inner side of the hole while the outer side undergoes larger elongation due to the specimen rotation, therefore the hoop strain measured by HER corresponds to the deformation in material on the inner side.

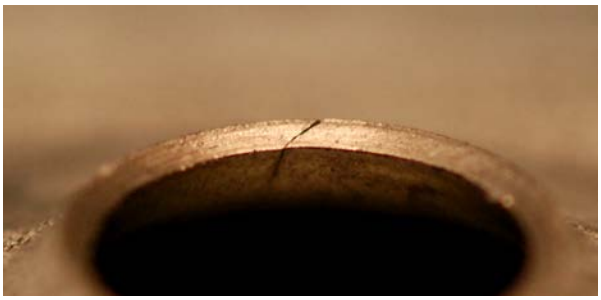

Fig. 21 No obvious localized necking around fracture

However, in tension test on central hole specimen strains is highly localized within the specimen and the hole edge undergoes non-uniform stretch. There is no such measurement as hole expansion ratio to measure the stretch limit. To quantitatively compare results with hole expansion tests, it is more reasonable to use the local strain at critical area on the hole edge where fracture initiates, which is also the maximum strain, as a benchmark of the fracture limit instead of using average hoop strain.

At the same time, DIC is not capable of obtaining strain right at the hole edge from test results due to the inherent constraints of the tool (Vic-2D 2009). Considering the deformation is highly localized and strain gradient is significant within the critical area, curve fitting and extrapolation is introduced to obtain a more accurate strain at hole edge. To do this, firstly the local strain component in tensile direction is extracted from DIC at different locations along the red dashed line marked in Fig. 22, which corresponds to the middle of the specimen with minimum cross section area. Then the strain distribution is fitted by a third order polynomial function to estimate the strain at hole edge by extrapolation. One typical test result is shown in Fig. 23. In current study the first data point obtained is 0.5mm away from hole edge and that point is taken as radial position reference.

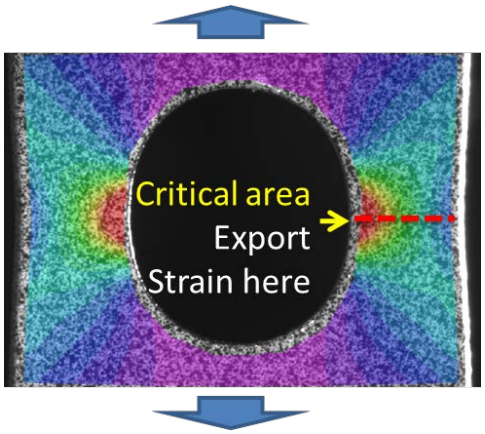

Fig. 22 Logarithmic axial strain contour measured by 2D DIC on last frame before fracture of central hole specimen

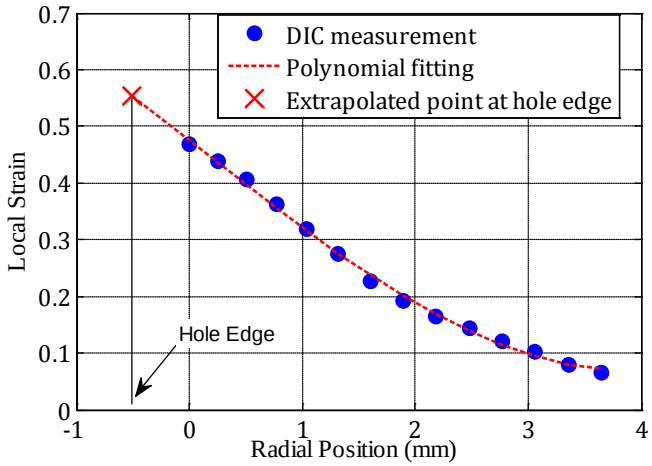

Fig. 23 Strain distribution and extrapolation of one hole expansion test

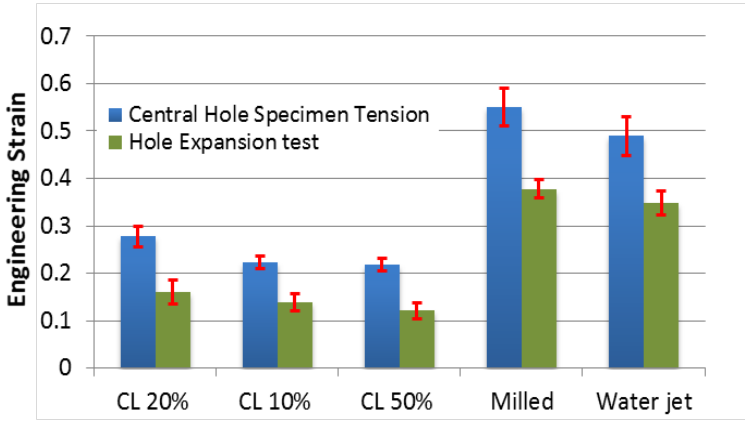

Fig. 24 Summary of strain at fracture. For HET the strain is taken from HER. For central hole specimen tension the strain is taken as the maximum local surface strain at the hole edge. The red tag over each bar denotes the standard deviation of corresponding test results

The local surface strain extrapolated for each tests are then summarized together with HET results in Fig. 24. Qualitatively speaking, hole expansion test and tension test on central hole specimen shows the same trend of strain at fracture for different machining technique. The local strain reported in tension on central hole specimen is generally higher than HER value. One important reason may be the fact that HER measures the inner side of the hole which undergoes less stretching compared with the outer side.

The local surface strain used in current study is only one bench mark of the many candidates that could be used to measure edge stretchability. Other options may include the displacement at failure as plotted in Fig. 14b, or the maximum strain within the specimen at the hole edge in the middle of the thickness direction, which needs a hybrid experimental and numerical method to measure.

6.3. FE prediction of HER without any pre-damage

As defined in Eq.9 the measurement of HER needs the inner diameter of the hole. The inner diameter is measured when the first through thickness fracture is developed. In current study, the element deletion technique was enabled and the first through thickness crack is denoted by the first row of elements deleted throughout the thickness. As illustrated by Fig. 25, nodes from the inner side of the edge in contact with the punch head is chosen to measure the inner

diameter. HER predicted by the simulation is 42.6%, which is very close to the testing results of 37% of milled specimen.

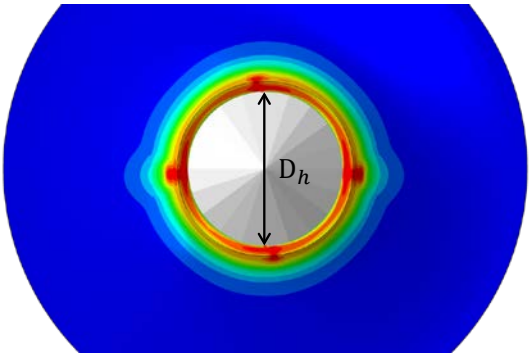

Fig. 25 Inner diameter measurement after first through thickness crack develops, color code is damage indicator

However such a model does not account for the pre-damage or strain hardening caused by sheet blanking process, therefore cannot predict the HER valued of punched holes. For accurate prediction of HER of punched holes, a two stage simulation that first models hole punching process and then simulate the hole expansion process is needed; or a model that includes the pre-damage and strain hardening from blanking process may also provide a solution.

6.4. More experimental observation

The post-test examination of the hole circumference revealed many interesting findings.

For punched specimen, there are many cracks initiating at the same time at different places around the edge. Only a few of them will develop into major cracks. Test is stopped when one major crack developed through thickness. This phenomenon is not observed in tests on milled specimen or water jet cut specimen. For milled specimen and water jet cut specimen, only one crack initiates and then develops throughout thickness, as shown in Fig. 26. Other parts of the hole edge are crack free if one stop the test immediately after the first crack develops. However, further loading will also result in multiple cracks.

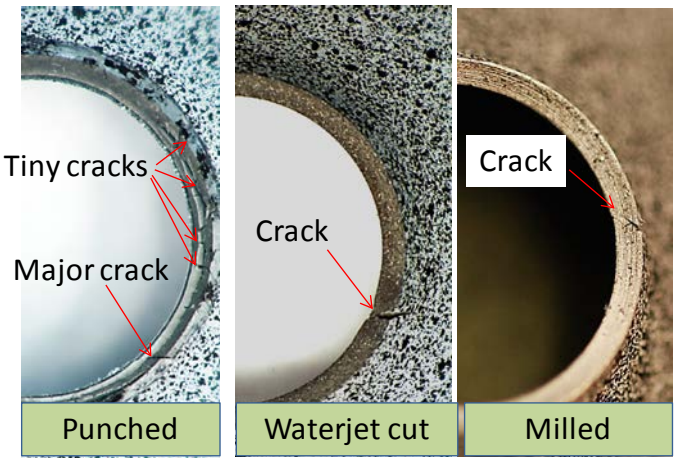

Fig. 26 Crack distribution for different type of edge

Fig. 27 shows the crack orientation in hole expansion tests on all three different types of specimen. Slant crack is found to be at about 45 degree in thickness direction for all cases, while in the radial direction the propagation is a little more complicated. On milled specimen, all cracks propagates straight forward in radial direction. In water jet cut specimen, both slant crack and straight crack are observed.

In punched specimen the case is quite different. Many cracks develops at the same time and all propagate in about 45 degree to the radial direction. Those multiple cracks form a periodic crack pattern that quite resembles shear band field at a round edge predicted by McClintock (1971) (Fig. 28). The orientation of crack is affected by many factors including stress state (Bai, 2008), material softening due to damage accumulation (Li and Wierzbicki, 2010), etc.

Fig. 27 Crack orientation and propagation in hole expansion tests

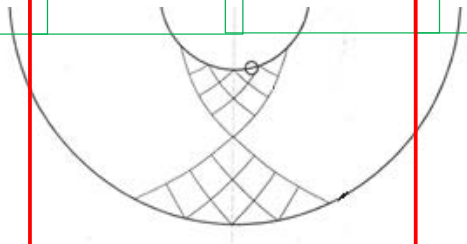

Fig. 28 Shear band field at a round edge, (McClintock 1971)

6.5. Finite element analysis of crack initiation and propagation

It's observed from hole expansion test on a milled specimen that usually one crack initiates in the beginning (Fig. 26). When the hole is further expanded another three cracks will follow and a total of four cracks will grow to open the hole (Fig. 29a). This observation is accurately captured by parallel numerical simulation.

Fig. 29c-e shows the evolution of damage indicator in the hoop direction at the edge. The variable θ is measured clockwise from horizontal axis x as shown in Fig. 29b. Rolling direction of the material is aligned perpendicular to axis x. Damage indicator is taken from elements at the edge on the upper surface on the specimen.

At the beginning the damage indicator distribution is quite uniform everywhere (Fig. 29c). When hole expansion proceeds the curves become waving around the hole edge. It is obvious there are four wave crests around the whole edge: two higher crests at $\theta = 0$ and $\theta = \pi$, another two relatively lower crests at $\theta = 0.5\pi$ and $\theta = 1.5\pi$.

When the maximum damage reaches 0.8, a localization happens. Damage accumulation concentrates at $\theta = 0$ and $\theta = \pi$, where two sharp peaks in the curve are formed corresponding to the first two cracks on specimen(Fig. 29d).

Further loading on the specimen will result in another two cracks at $\theta = 0.5\pi$ and $\theta = 1.5\pi$ as illustrated by Fig.29e. It also observed that after cracks are formed, there is no further damage accumulation outside the cracks, meaning that during further loading plastic deformation concentrates in the cracking zone. After four cracks are fully formed, they would propagate in radial direction. No additional cracks are formed afterwards.

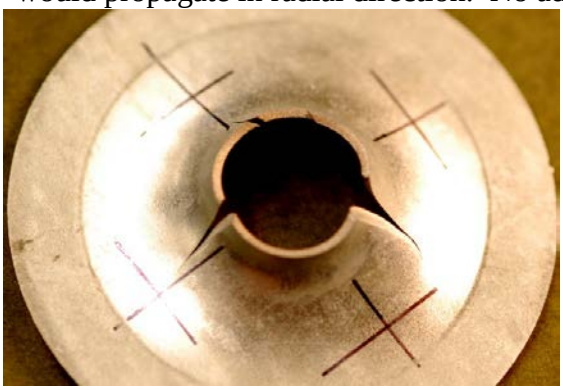

(a) Crack distribution in testing

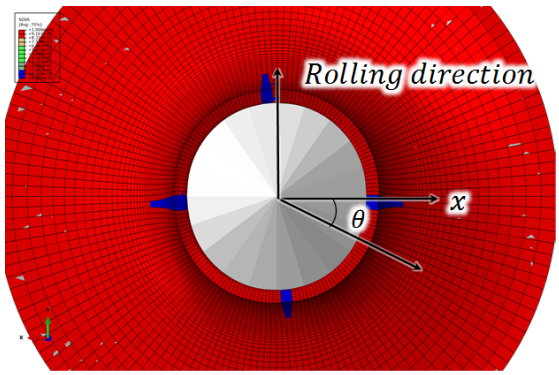

(b) Material orientation and angle, crack distribution in simulation

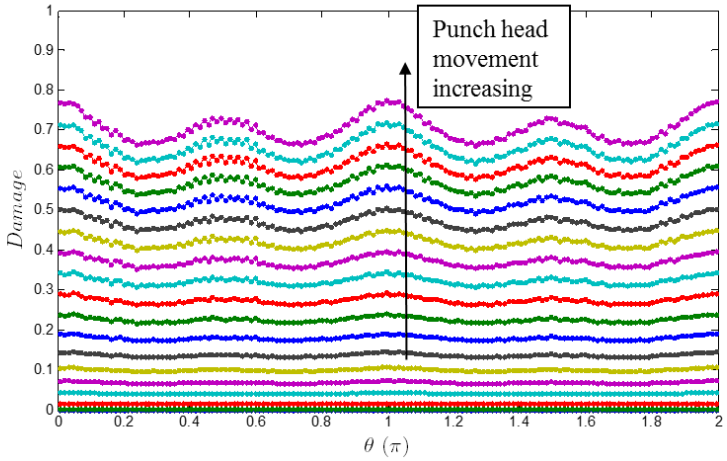

(c) Before localization and crack happens, damage indicator waves along hole edge

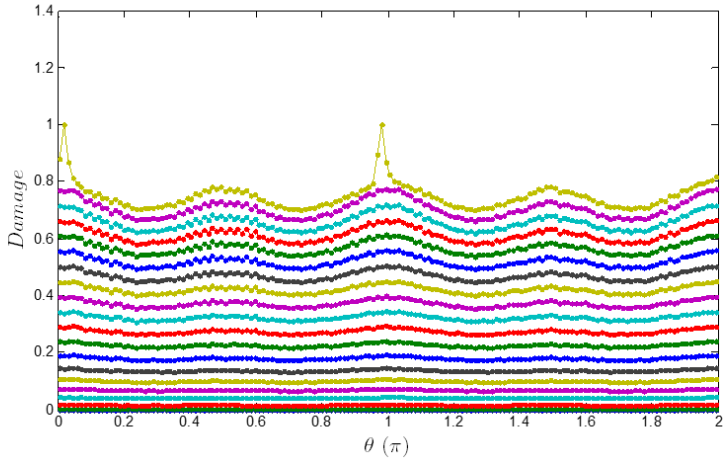

(d) Localization happens, damage accumulates faster at two points and lead to the first two crack

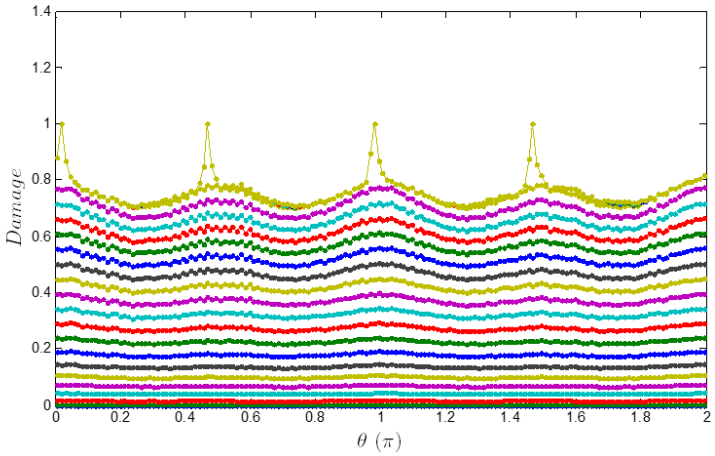

(e) The third and fourth crack happens at $\theta = 0.5\pi$ and $\theta = 1.5\pi$ when one further expand the hole

Fig. 29 Damage accumulation and crack initiation during hole expansion test. Modeling with Hill 48 yield condition and associated flow rule

It is very significant that the present model of a crack-free body predicts correctly a sequence of crack formation and the number of cracks.

It is quite interesting that despite the perfect axisymmetric geometry and loading condition in the model, the damage accumulation shows periodic variation along the edge. This variation comes from the anisotropy of the sheet metal. For comparison, simulation assuming isotropic material was carried out and the damage evolution is presented below. Definition of angle θ is the same as before. The distribution is only plotted for half of the circle.

After introducing isotropic material, the periodic waving in damage indicator distribution is eliminated (Fig. 30a). "Waving" of the curves is caused by accumulation of random numerical error. Damage will reach a level of almost 0.8 all around the hole edge and suddenly localization happens at multiple places (Fig. 30b). Six cracks initiate almost at the same time (half circle). These cracks are evenly distributed along hole edge. It needs to be point out that the number of 12 cracks predicted here is not physically observed because of the isotropic material assumption. At the same time, the number of cracks is quite sensitive to lots of factors including numerical calculation accuracy, mesh size, material property, etc.

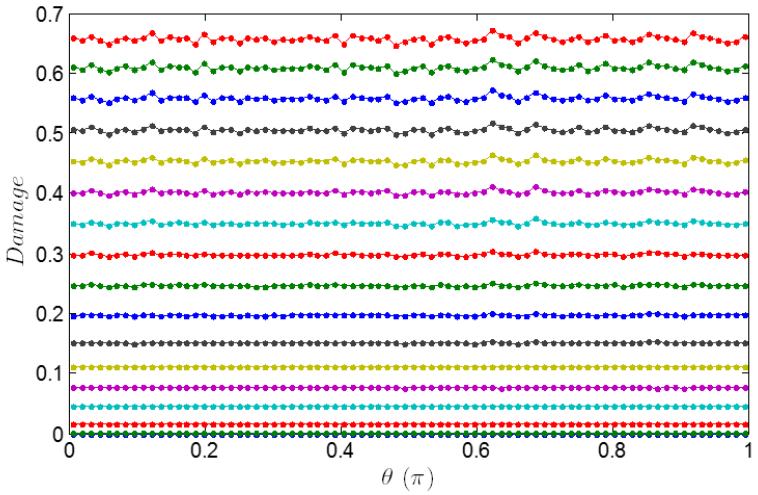

(a) Before localization and crack happens, damage indicator almost constant along the hole edge

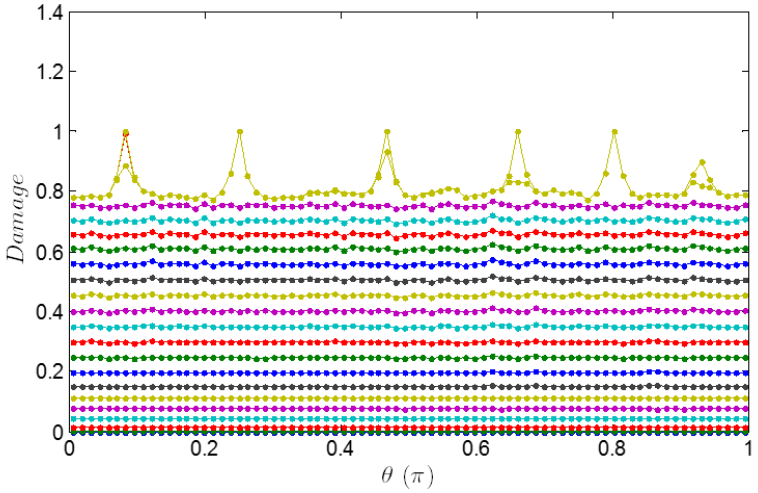

(b) Localization happens and crack initiates at 6 places almost at the same time

Fig. 30 Damage accumulation and crack initiation during hole expansion test. Modeling with isotropic material and associated flow rule

7. Summary and conclusions

In the present study, the edge fracture of a DP780 AHSS sheet is studied using both experimental methods and FE simulations. The follow conclusions can be drawing from this investigation:

1) Hill'48 plasticity model is sufficient to model the anisotropic plastic deformation of the present DP780 sheet under multi-axial loadings. It serves as a solid basis for all subsequent ductile fracture simulations.

2) The ductile fracture properties of the present AHSS sheet in its virgin crack-free state is fully characterized using a MMC fracture model. The model is calibrated with a testing program covering eight distinct stress states. It has been shown that the MMC model provides satisfactory description of the ductile fracture behavior of the present sheet under various stress states.

3) The hole expansion testing program is carried out to investigate the edge fracture behaviors of the present sheet. The HET results suggest that milled hole yields the highest HER of 38% while water jet cut hole has a little smaller HER of 35%. Punched specimen generally has a much lower HER of 12% ~ 16%. It is also confirmed that hole punched with die clearance $CL = 20\%$ has the highest HER.
4) A novel central hole specimen tension test is introduced for edge fracture study. The strain concentration at hole edge favors a fracture initiation at the edge, rendering this test a good candidate for edge fracture study. Test results show the same trend as discovered in HET test, which is milled specimen has the highest fracture limit and punched specimen generally has much lower one. Among all punched specimen, the ones with die clearance $CL = 20\%$ yields highest stretch limit. The test is relatively easier in terms of that it requires a simple uniaxial tension test on a flat specimen. It need to be point out that due to the non-uninform strain field, local strain at the critical area of fracture should be used as a measure of the residual ductility rather than an average hoop strain. DIC or even hybrid numerical and experimental method are needed to determine local strain.
5) FE simulation of hole expansion test on un-cracked material gives a good prediction of the load displacement response as well as of the deflection distribution in radial direction. The simulation also predicts HER with good accuracy. Note that in current study specimens with carefully milled hole are assumed to be the un-cracked material.
6) In the current study, FE simulation did not take pre-damage caused by punching/trimming process into consideration. The MMC model used is calibrated from virgin material and could not predict HER in punched specimen accurately. A two-step simulation that continues hole punching with hole expansion, or a model includes pre-damage and residual strain into consideration is needed to tackle this problem.
7) The present simulation explained the mechanism of the crack initiation, propagation and arrest. The final count of the number of cracks agrees well with experimental observations.

Future works will include a detailed two stage simulation that takes the punching process into consideration. The punching process will be simulated to find out how trimming causes change to the properties in SAZ. The hole expansion simulation will then continue on the punched hole. Also experimental check on the blanking process would also be of great interest. The out-of-plane shearing may require different damage accumulation mechanism for the subsequent hole expansion process and need further investigation.

8. Acknowledgements

The authors are grateful to Voestalpine for supplying sheet metal for testing. Dr. Ming F. Shi at US Steel is gratefully acknowledged for helping punching the hole and for valuable discussion. Thanks are also due to Hyperworks for kindly providing Hypermesh that prepared some of the models for Finite Element simulation in current study.

References

Abaqus, 2010. Reference Manual v6.10. Dassault Systèmes Simulia Corp.
Bai, Y., 2008. Effect of loading history in necking and fracture, Mechanical Engineering. Massachusetts Institute of Technology, Cambridge.
Bai, Y., Wierzbicki, T., 2010. Application of extended Mohr-Coulomb criterion to ductile fracture. Int J Fracture 161, 1-20.
Beese, A.M., Luo, M., Li, Y.N., Bai, Y.L., Wierzbicki, T., 2010. Partially coupled anisotropic fracture model for aluminum sheets. Engineering Fracture Mechanics 77, 1128-1152.
Butcher, C., Anderson, D., Worswick, M., 2013. Predicting Failure during Sheared Edge Stretching Using a Damage-Based Model for the Shear-Affected Zone. SAE International Journal of Materials & Manufacturing 6, 304-312.
Chiriac, C., Chen, G., 2008. Local Formability Characterization of AHSS–Digital Camera Based Hole Expansion Test Development, Best in Class Stamping, Proceedings of the International Deep Drawing Research Group (IDDRG) 2008 Conference. Swedish Deep Drawing Research Group, Olofström, Sweden, pp. 81-91.
Chiriac, C., Shi, M., 2013. Studies on Edge Strain Hardening Produced by Trimming Operations. SAE SP.
Dunand, M., Mohr, D., 2010. Hybrid experimental-numerical analysis of basic ductile fracture experiments for sheet metals. Int J Solids Struct 47, 1130-1143.
Dunand, M., Mohr, D., 2011. On the predictive capabilities of the shear modified Gurson and the modified Mohr-Coulomb fracture models over a wide range of stress triaxialities and Lode angles. J Mech Phys Solids 59, 1374-1394.
Hill, R., 1948. A theory of the yielding and plastic flow of anisotropic metals. Proc. Roy. Soc. Lond. A 193, 281-297.
Hyun, D., Oak, S., Kang, S., Moon, Y., 2002. Estimation of hole flangeability for high strength steel plates. Journal of materials processing technology 130, 9-13.
ISO, 2008. Method of hole expanding test.
JFS, 1996. Method of Hole Expansion Test.
Konieczny, A., Henderson, T., 2007. 2007-01-0340 On Formability Limitations in Stamping Involving Sheared Edge Stretching. SAE SP 2103, 41.
Li, Y., Wierzbicki, T., 2010. Prediction of plane strain fracture of AHSS sheets with post-initiation softening. Int J Solids Struct 47, 2316-2327.
Luo, M., Dunand, M., Mohr, D., 2012. Experiments and modeling of anisotropic aluminum extrusions under multi-axial loading - Part II: Ductile fracture. Int J Plasticity 32-33, 36-58.
Luo, M., Wierzbicki, T., 2010. Numerical failure analysis of a stretch-bending test on dual-phase steel sheets using a phenomenological fracture model. International Journal of Solids and Structures 47, 3084-3102.
McClintock, F.A., Argon, A.S., 1971. Mechanical behavior of materials. Addison-Wesley Pub. Co.
Pathak, N., Butcher, C., Worswick, M., 2013. Influence of the sheared edge condition on the hole expansion of dual phase steel, IDDRG 2013 Conference. Swedish Deep Drawing Research Group, Olofström, Sweden.
Shi, M., Chen, X., 2007. Prediction of Stretch Flangeability Limits of Advanced High Strength Steels using the Hole Expansion Test. SAE SP 2103, 383.
Shih, H.-C., Chiriac, C., Shi, M.F., 2010. The effects of AHSS shear edge conditions on edge fracture, ASME 2010 International Manufacturing Science and Engineering Conference, Pennsylvania, USA.
Stanton, M., Bhattacharya, R., Dargue, I., Aylmore, R., Williams, G., 2011. Hole Expansion of Aluminum Alloys for the Automotive Industry, AIP Conference Proceedings, p. 1488.

Wu, X., Bahmanpour, H., Schmid, K., 2012. Characterization of mechanically sheared edges of dual phase steels. Journal of materials processing technology 212, 1209-1224.

Appendix A: Additional load displacement response of tests for fracture calibration

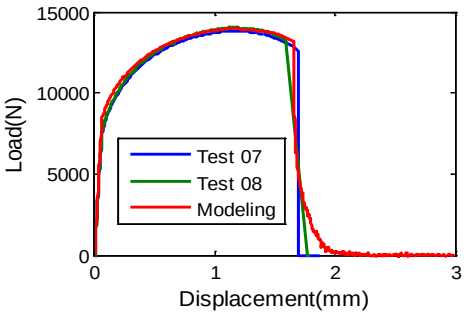

(a) Notched specimen, R=6.67mm

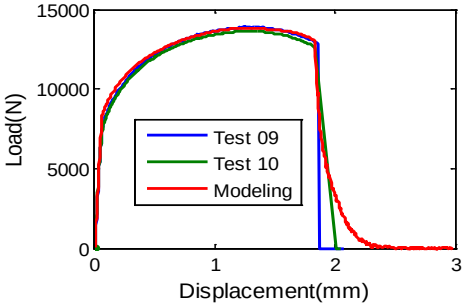

(b) Notched specimen, R=10mm

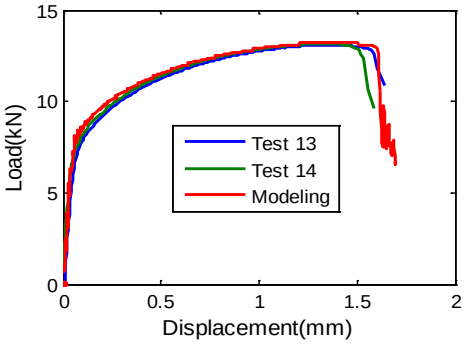

(c) Central hole specimen tension

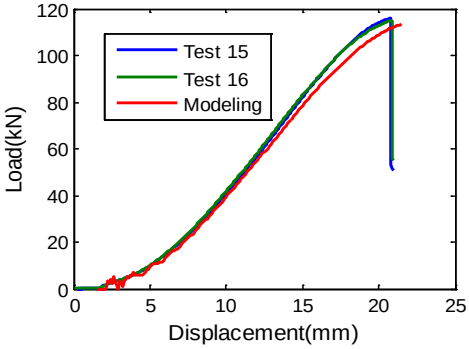

(d) Equi-biaxial tension test

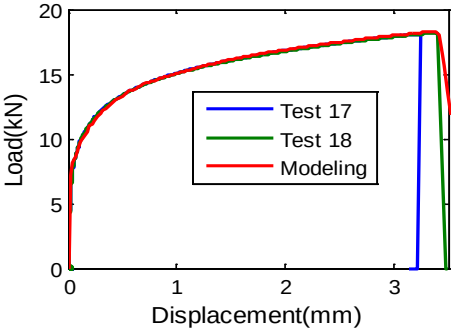

(e) pure shear on butterfly specimen

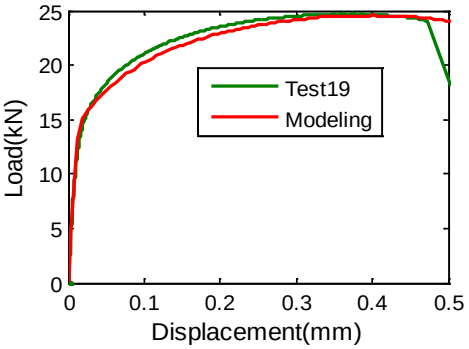

(f) simple tension on butterfly specimen

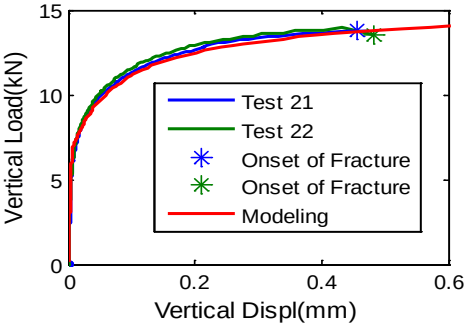

(g) 45°combined loading on butterfly specimen, vertical direction

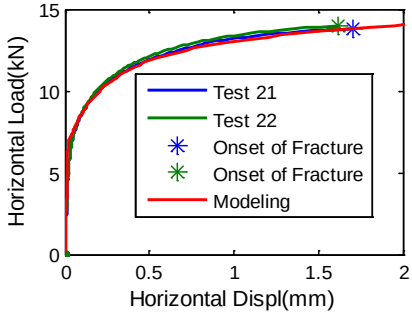

(h) 45°combined loading on butterfly specimen, horizontal direction

Fig. A1 Load displacement curves of various tests used in fracture model calibration, results from testing and simulation

Appendix B: Analytical solution of hole expansion test

Observation over specimen cross section after test shows a logarithmic deformed shape (Fig. B 1a). A comparison between the scanned profile and a logarithmic curve (blue curve in Fig. B 1b) lends additional support to this approximation. Therefore, a logarithmically deformed specimen profile was assumed for the derivation of an approximate analytical solution for the hole expansion process.

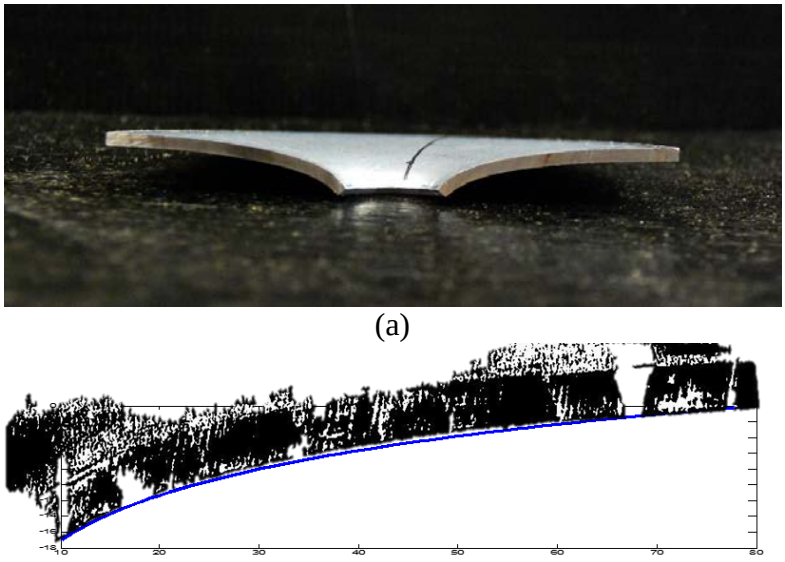

(a)

(b)

Fig. B 1 Specimen profile after hole expansion test, (a) View on specimen cross section, (b) Specimen profile taken from scanner compared with logarithmic curve

In present study, specimen thickness to radius ratio is small t/R=0.064. For simplicity, a membrane assumption is introduced and the contribution of the bending resistance is disregarded. Considering axial symmetry, a cylindrical coordinate system is established with z axis (named w, denoting deflection in current case) coaxial with conical punch head, and r axis pointing in the radial direction of test specimen (Fig. B 2). The maximum displacement at $r = r_1$ is denoted as w_0. At the clamped edge $r = r_2$, the deflection is zero. Therefore, the deflection distribution can be described by Eq.B1.

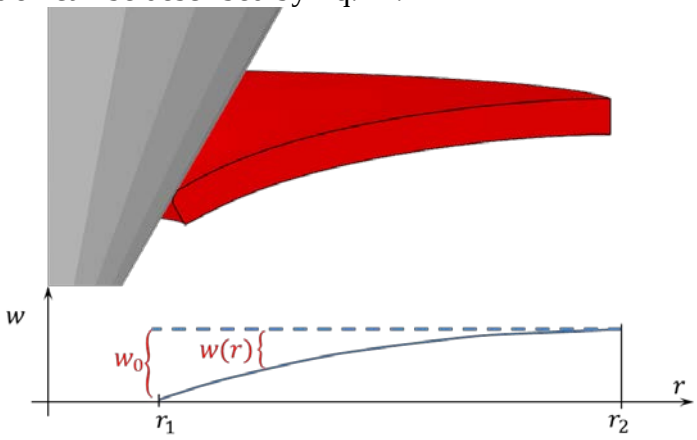

Fig. B 2 Coordinate definition for analytical formulation

$$w(r) = w_0\left[1 - \frac{\ln\left(\frac{r}{r_1}\right)}{\ln\left(\frac{r_2}{r_1}\right)}\right] \tag{B1}$$

Assuming there is no friction between punch head and specimen, considering membrane assumption there is no deformation in radial direction, and the radial strain is zero

$$\therefore \quad \epsilon_r = u_r' + \frac{1}{2}(w')^2 = 0 \tag{B2}$$

where $(*)'$ denotes $\partial(*)/\partial r$. Introducing Eq. (12) into Eq.B2, one gets

$$\therefore \; u_r' = -\frac{1}{2}(w')^2 = -\frac{1}{2}\left(\frac{\frac{w_0}{r}}{\ln\left(\frac{r_2}{r_1}\right)}\right)^2 \tag{B3}$$

After integration,

$$\therefore \; u(r) = \frac{w_0^2}{2\eta^2}\frac{1}{r} + C \tag{B4}$$

where $\eta = ln(r_2/r_1)$.

Considering boundary condition at $r = r_2$, $u(r_2) = 0$,

$$\therefore \; u(r) = \frac{w_0^2}{2\eta^2}\left(\frac{1}{r} - \frac{1}{r_2}\right) \tag{B5}$$

Therefore hoop strain distribution can be expressed as:

$$\epsilon_\theta = \frac{u(r)}{r} = \frac{1}{2\eta^2}\left(\frac{w_0}{r_1}\right)^2\frac{r_1}{r}\left(\frac{r_1}{r} - \frac{r_1}{r_2}\right) \tag{B6}$$

This analytical solution is plotted as red dashed curve in Fig. B 3 and compared with numerical simulation results for a chosen value of central deflection $w_0 = 5mm$. A reasonably good agreement is obtained.

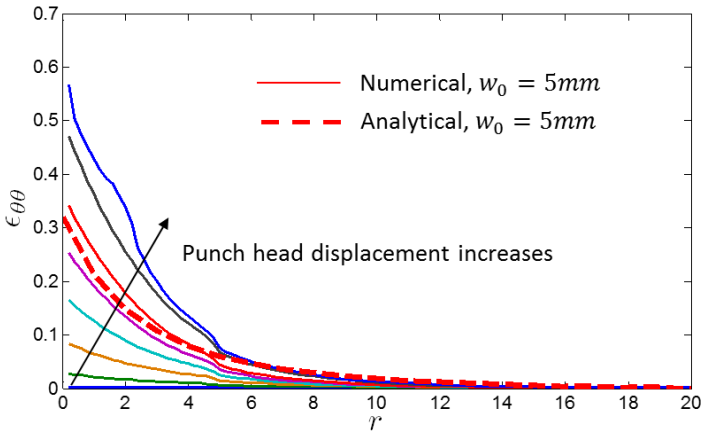

Fig. B 3 Hoop stress distribution and evolution, comparison between numerical simulation and analytical solution at $w_0 = 5mm$

To calculate the reaction force of punch head as a function of displacement, the Principle of Virtual Work (PVW) is introduced (Eq.B7).

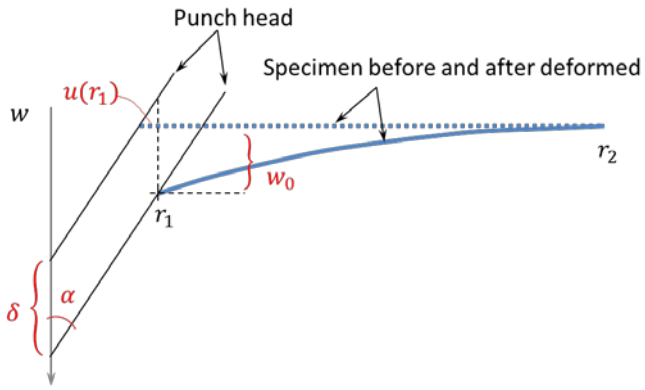

Fig. B 4 Relationship between punch head movement δ and specimen deflection w_0

$$2\pi h \int_{r_1}^{r_2} (\sigma_\theta \dot{\epsilon}_\theta + \sigma_r \dot{\epsilon}_r)\, r dr = P\dot{\delta} \tag{B7}$$

where h denotes the thickness of the specimen and δ is the punch deisplacement

According to membrane assumption, $\sigma_r \dot{\epsilon}_r = 0$. Also the material is assumed to be rigid-perfect-plastic, where σ_0 is the energy equivalent flow strength, defined by:

$$\sigma_0 = \frac{1}{\varepsilon_1} \int_0^{\varepsilon_1} \sigma(\varepsilon) \mathrm{d}\varepsilon \tag{B8}$$

where $(0, \varepsilon_1)$ denotes the range of strains over which the averaging of flow strength is made. In uniaxial test, the maximum uniaxial strain is limited by the onset of localized necking, so $\varepsilon_1 = \mathrm{n}$, where n is the exponent of the Swift law hardening law. However, in the hole expansion problem there is no observable localized neck and the maximum strain to fracture is much higher, of the order of $\varepsilon_1 = 0.7$. Taking the amplitude A and the exponent n from Table 4, the flow stress calculated from Eq. 19 is $\sigma_0 = 1141\mathrm{MPa}$.
From Eq.B6 the strain rate $\dot{\epsilon}_\theta$ can be expressed as:

$$\dot{\epsilon}_\theta = \frac{\dot{u}(r)}{r} = \frac{w_0 \dot{w}_0}{\eta^2 r} \left(\frac{1}{r} - \frac{1}{r_2} \right) \tag{B9}$$

Then Eq. B7 is rewritten as:

$$P\dot{\delta} = 2\pi\sigma_0 h \frac{w_0 \dot{w}_0}{\eta^2} \int_{r_1}^{r_2} \left(\frac{1}{r} - \frac{1}{r_2} \right) dr = \frac{2\pi\sigma_0 h w_0 \dot{w}_0}{\eta^2} \left(\eta - \frac{r_2 - r_1}{r_1} \right) \tag{B10}$$

The relation between $\dot{w}_0$ and $\dot{\delta}$ to get an expression for reaction force P is defined by the geometry of the problem see Fig. 24:

$$u(r_1) = (\delta - w_0) \tan \alpha \tag{B11}$$

$$\therefore \dot{\delta} = \left(\frac{w_0}{\eta^2 \tan\alpha}\frac{r_2 - r_1}{r_1 r_2} + 1\right)\dot{w}_0 \tag{B12}$$

Substituting this relation into Eq.(21) one can find the expression for reaction force P as:

$$\mathrm{P} = \frac{2\pi\sigma_0 h r_2 \cdot \dfrac{\eta - \dfrac{r_2 - r_1}{r_1}}{\eta^2} \cdot \dfrac{w_0}{r_2}}{\dfrac{w_0}{r_2} \cdot \dfrac{r_2 - r_1}{r_1} \cdot \dfrac{1}{\eta^2 \tan\alpha} + 1} \tag{B13}$$

In present case $r_2 = 25\text{mm}$, $r_1 = 5\text{mm}$, $h = 1.6\text{mm}$, $\alpha = 30°$ and $\sigma_0 = 1141\text{MPa}$. The analytical solution is then compared with test result in Fig. B 5. The comparison of analytical solution and measured load shows good correlation over 2/3 of the considered range of the punch displacement and then starts to deviate.

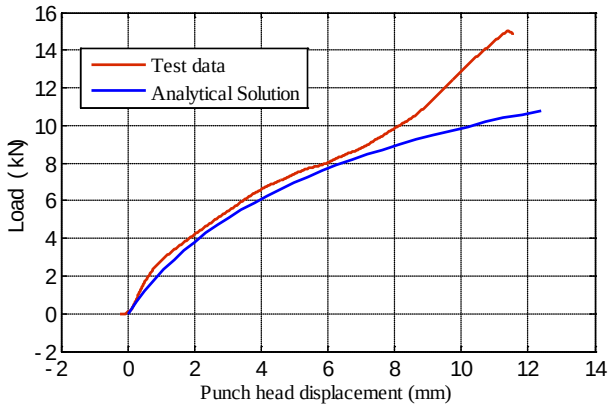

Fig. B 5 Load displacement curve of hole expansion test, testing vs. analytical solution